Petrology and ^{40}Ar-^{39}Ar dating of paragneisses from the Devrekani Massif (Central Pontides, Northern Turkey): Implications for the Jurassic high-T metamorphism in an extensional tectonic environment

Journal Item

Petrology and ^{40}Ar-^{39}Ar dating of paragneisses from the Devrekani Massif (Central Pontides, Northern Turkey): Implications for the Jurassic high-T metamorphism in an extensional tectonic environment

Mehmet Ali Gücer, Mehmet Arslan, Okay Çimen, Sarah C. Sherlock

PII: S1367-9120(19)30240-8
DOI: https://doi.org/10.1016/j.jseaes.2019.103888
Article Number: 103888
Reference: JAES 103888

To appear in: *Journal of Asian Earth Sciences*

Received Date: 11 December 2018
Revised Date: 1 June 2019
Accepted Date: 14 June 2019

Please cite this article as: Ali Gücer, M., Arslan, M., Çimen, O., Sherlock, S.C., Petrology and ^{40}Ar-^{39}Ar dating of paragneisses from the Devrekani Massif (Central Pontides, Northern Turkey): Implications for the Jurassic high-T metamorphism in an extensional tectonic environment, *Journal of Asian Earth Sciences* (2019), doi: https://doi.org/10.1016/j.jseaes.2019.103888

Petrology and ^{40}Ar-^{39}Ar dating of paragneisses from the Devrekani Massif (Central Pontides, Northern Turkey): Implications for the Jurassic high-T metamorphism in an extensional tectonic environment

Mehmet Ali Gücer[a,*], Mehmet Arslan[b], Okay Çimen[c], Sarah C. Sherlock[d]

[a] *Department of Geological Engineering, Gümüşhane University, TR-29000, Gümüşhane, Turkey*

[b] *Department of Geological Engineering, Karadeniz Technical University, TR-61080 Trabzon, Turkey*

[c] *Rare Earth Elements Application and Research Center, Munzur University, TR-62000 Tunceli, Turkey*

[d] *School of Physical Sciences, STEM Faculty, The Open University, Walton Hall, Milton Keynes, MK7 6AA, UK*

Abstract

The Devrekani Massif in the northern part of the Central Pontides (Northern Turkey) provides important clues to the regional tectonics and geodynamic processes associated with Jurassic high grade metamorphic conditions. This study reports new paragenetic assemblages, mineral compositions, whole-rock geochemistry and ^{40}Ar-^{39}Ar geochronological data from the paragneisses in the massif, and, discusses the *P–T* conditions and geodynamic implications of the Jurassic metamorphism during continental extension in the Central Pontides. Upper amphibolite to lower granulite facies paragneisses form one of the main lithological units in the massif. Within these, there are five different mineral parageneses with diagnostic mineral assemblages of: quartz, K-feldspar ($An_{0-1}Ab_{4-26}Or_{73-96}$), plagioclase ($An_{18-35}$), biotite [($X_{Phl}$: 0.28-0.57; $Mg/(Mg+Fe^{2+})$: 0.33-0.61)], sillimanite, cordierite [($Mg/(Mg+Fe^{2+})$: 0.48-0.71)] and garnet ($Alm_{43-80}Grs_{0-18}Prp_{5-23}And_{0-4}Sps_{10-33}$) with minor hercynite. Based on Na-in-Crd thermometry and GASP barometry results, the peak

* Corresponding author.
E-mail address: maligucer@gmail.com (M.A. Gücer)

metamorphic conditions are 775±25°C and 6±1 kbar in the massif. The field relations, petrography and bulk chemical data suggest that the paragneisses, derived from shale-wackestone and pelitic sedimentary protoliths, are typical rock lithologies of an active continental margin. They display enrichments in LILE over HFSE, coupled with negative Nb and Ti anomalies, which are geochemical signatures of subduction-related sources. It is likely that the peak metamorphism took place during the Middle–Upper Jurassic period (*ca.* 174–156 Ma), suggesting that the metamorphic rocks cooled to 300-350°C at *ca.* 156 Ma. The mineral assemblages reveal that the prograde history passed from sillimanite zone conditions up to the cordierite-garnet-K-feldspar zone. The petrological and geochronological data indicate that the protoliths are related to multiple sources such as volcano-sedimentary successions. We conclude that the Devrekani Massif represents the products of pre-Jurassic sedimentation, and Permo-Carboniferous continental arc magmatism, overprinted by Jurassic metamorphism.

Keywords: Central Pontides, Devrekani Massif (Northern Turkey), Geochronology, Geothermobarometry, Jurassic metamorphism, Paragneisses

1. Introduction

Turkey (or Anatolia) formed from the amalgamation of three micro-plates, or terranes, during the closure of Neotethyan oceanic branches (e.g., Şengör and Yılmaz, 1981; Göncüoğlu et al., 1997). From north to south (Fig. 1a), these tectonic units are: the Istanbul-Zonguldak Terrane (IZT), the Sakarya Composite Terrane (SCT) and the Anatolide-Tauride Terrane (ATT). In the north, the IZT and SCT are separated by the Intra-Pontide Suture Belt (IPSB; e.g., Göncüoğlu et al., 2014; Çimen et al., 2016) whereas the Izmir-Ankara-Erzincan Suture Belt (IAESB; the northern branch of Neotethys), which stretches from the Aegean Sea

to the Lesser Caucasus, represents a boundary between the SCT and ATT (e.g., Aldanmaz et al., 2008; Parlak et al., 2013; Çimen and Öztüfekci, 2018). In the south, the ATT and the Arabian Platform are separated by the southern branch of Neotethys (e.g., Yılmaz and Yılmaz, 2013; Akmaz et al., 2014; Parlak, 2016).

The IZT is characterized by the Neoproterozoic crystalline basement (e.g., Bolu Massif; Ustaömer et al., 2005), which is unconformably overlain by the Paleozoic and Mesozoic cover units (e.g., Dean et al., 1997; Chen et al., 2002; Özgül, 2012; Okay et al., 2015). The Paleozoic cover units are locally cut by Permian granitoids (e.g., Şahin et al., 2009; Aysal et al., 2018). However, in contrast, the SCT is composed of Devonian magmatic rocks, for example, the Çamlık and Karacabey plutons (e.g., Aysal et al., 2012; Sunal, 2013); Variscan units, for example, the Söğüt, Devrekani and Pulur metamorphic rocks (e.g., Topuz et al., 2004; Nzegge, 2008; Ustaömer et al., 2012; Okay and Topuz, 2017) and the Cimmerian Karakaya complex basement (e.g., Okay and Göncüoğlu, 2004; Sayıt et al., 2010; Ustaömer et al., 2016), which is overlain by the Alpine cover units (Okay et al., 2006; Göncüoğlu, 2010). The Central Pontides in Northern Turkey is one of the most complex areas in the Black Sea region and comprises the IZT, the SCT and a subduction-accretion complex known as the Central Pontide Supercomplex (Okay et al., 2013), or, as the Central Pontide Structural Complex (Tekin et al., 2012), representing the remnants of the IPSB (e.g., Frassi et al., 2017; Çimen et al., 2018).

During the Late Paleozoic, the Variscan orogeny formed in the Appalachians and Central Europe due to the collision of Gondwana-derived terranes with Laurasia (Okay and Topuz, 2017, and references therein). This resulted in the formation of many Variscan basement units in the Black Sea region including the Balkans, Pontides and the Caucasus (Okay and Topuz, 2017). The main Variscan basement units in the SCT are represented by the Söğüt

metamorphic rocks in the west (e.g., Ustaömer et al., 2012), the Devrekani Massif in the north (e.g., Okay et al., 2014) and the Pulur Complex in the east (e.g., Topuz et al., 2004).

In the Central Pontides, the Variscan basement units are the Devrekani Massif, the Permo-Carboniferous Sivrikaya and the Deliktas Granitoids (Nzegge, 2008; Okay et al., 2014, Gücer et al., 2016). Of these, the Devrekani Massif consists of cordierite and sillimanite-bearing gneisses, indicating low pressure-high temperature conditions. Although, the age of metamorphism from the Devrekani Massif has been reported as being Middle Jurassic by Okay et al. (2014) and Gücer et al. (2016), the metamorphic evolution of this unit has not yet to be fully established.

This study reports new mineralogical, petrochemical and geochronological data for paragneisses from the Devrekani Massif in order to better evaluate their petrogenetic and geodynamic evolution. It will also provide useful insights for the ongoing discussions in relation to the evolution of the Central Pontides and the Black Sea region, particularly for the Middle Jurassic period.

2. Geological background

2.1. Regional geology

The pre-Jurassic units in the Central Pontides are represented by several basement units such as the Devrekani Massif, Geme Complex and Permo-Carboniferous Deliktaş-Sivrikaya Granitoids (e.g., Nzegge, 2008; Okay et al., 2014, Gücer et al., 2016, Çimen et al., 2018; Fig. 1b). The Devrekani Massif and the Geme Complex are mainly composed of orthogneisses, micaschists, marble, and metamorphosed ophiolite slices. The Küre Complex has overthrust these basement units, and has been defined as dismembered ophiolite-bearing thrust-imbricated deep-sea sediments (Ustaömer and Robertson, 1999). It pre-dates the late middle Jurassic, and is likely to be between Late Triassic and Middle Jurassic in age (Kozur et al.,

2000; Yılmaz and Yılmaz, 2013; Okay et al., 2015). The Küre Complex is unconformably overlain by the Bürnük Formation (Middle-Late Jurassic) in the Central Pontides (Okay et al., 2015; Hippolyte et al., 2016).

Widespread Middle Jurassic continental arc magmatism, for example the Çangaldağ and Karaman plutons, cuts the basement units and the Küre Complex at several locations (Okay et al., 2014; Çimen et al., 2017, 2018; Ballato et al., 2018). This represents an active arc above the subducting slab of the Jurassic ocean beneath the accreted basement of the Central Pontides. Notably, the isotope data from the Çangaldağ Pluton, reveals that the arc magmatism may have incorporated partially melted Neoproterozoic/Mesoproterozoic crustal rocks (e.g., Devrekani Massif), which are a common feature in Gondwana-derived terranes (Çimen et al., 2017). The Jurassic arc-type volcanic rocks are also known in the Crimea region, which may have been derived from a subduction-related setting beneath the active margin of Eurasia (e.g., Meijers et al., 2010). Besides, similar Jurassic volcanic rocks with subduction-related geochemical characteristics have been reported in the Caucasus region (e.g., McCann et al., 2010).

Pre- to Late-Jurassic rocks in the Central Pontides are unconformably overlain by cover such as the Upper Jurassic İnaltı Unit, Lower Cretaceous Çağlayan Unit and also Tertiary units (e.g., Uguz and Sevin, 2007; Akdoğan et al., 2017).

2.2. Local geology

The Devrekani Massif in the north of the Kastamonu region covers an area of ~180 km^2 (Fig. 1c), and contains predominantly gneisses, marble, and to a lesser extent, amphibolites and quartzites. The mineral assemblage of gneisses is quartz, K-feldspar, plagioclase, biotite, sillimanite, cordierite and garnet, with minor Fe-Ti oxide, hercynite, and accessory minerals apatite and zircon. The gneisses are light to dark grey with a distinctive white and brown

weathering color, and the foliation is generally parallel to NE-SW and dips at 35°-70°. Their compositions suggest that the protoliths are mainly Neoproterozoic to Paleozoic sedimentary and magmatic rocks. The Middle-Jurassic granitoids that cross-cut the Devrekani Massif are syenogranite to granodiorite in composition (Yılmaz, 1980), and are 170-165 Ma in age (Nzegge, 2008).

3. Analytical techniques

3.1. Electron microprobe (EMP) analysis

Electron microprobe analysis of rock-forming minerals (garnet, sillimanite, cordierite, plagioclase, K-feldspar, biotite, hercynite and Fe-Ti oxide) were performed on 10 polished thin sections of representative paragneiss samples with a CAMECA SX-50 electron microprobe at the Elektronenstrahl-Mikrosonde Labor, Ruhr Universität (Bochum, Germany). The EMP is fitted with four wavelength-dispersive spectrometers (WDS) and one energy-dispersive spectrometer (EDS). Operating conditions were an accelerating voltage of 15 kV and a beam current of 15 nA. Counting times were 20 s on peak for Na, Mg, Al, Si, Ca, K, Ti, Mn and Fe. Natural and synthetic minerals were used as calibration standards, and detection limits were 0.02-0.06 wt% for the analyzed elements. A focused beam was applied to all phases except for micas, for which a slightly defocused beam was used. Mineral abbreviations used in the text, figures, and tables are from Whitney and Evans (2010).

3.2. Whole-rock geochemical analysis

Whole-rock geochemical analyzes of 18 representative paragneiss samples were carried out at ACME Analytical Laboratories Ltd., Vancouver (Canada). Samples were crushed into small chips of 0.1-1 cm using a jaw crusher and then powdered using a mild-steel mill. For major elements, samples were prepared with 0.2 g of rock powder fused with 1.5 g $LiBO_2$ and

dissolved in 100 ml of 5% HNO_3. For rare earth elements (REE) the samples were prepared with 0.25 g rock powder that was dissolved during multiple acid digestion steps. Loss on ignition (LOI) is the difference in weight before and after ignition at 1000°C. All major and trace element compositions were determined by inductively coupled plasma atomic emission spectroscopy (ICP-AES), with detection limits of approximately 0.01 to 0.1 wt% for major oxides, 0.1 to 10 ppm for trace elements. The REEs were analyzed by inductively coupled plasma mass spectrometry (ICP-MS), with detection limits of 0.01 to 0.5 ppm.

3.3. ^{40}Ar-^{39}Ar analysis

Biotite minerals from 3 representative paragneiss samples were dated at the ^{40}Ar-^{39}Ar and Noble Gas Laboratory, in the STEM Faculty at the Open University (UK). The infrared (IR) laser probe spot dating technique was used to analyze biotite, and the samples were prepared as 5x5 mm polished thick sections with approximately 250 μm in thickness. Samples were irradiated at the McMaster Nuclear Reactor, McMaster University, Canada, for 50 hours. Neutron flux was monitored using biotite mineral standard GA1550 which has an age of 98.8±0.5 Ma (Renne et al., 1998). The resulting J values ranged from 0.00758 to 0.00759 (error 0.000038; n= 3). The following correction factors were used: $(^{39}Ar/^{37}Ar)_{Ca}$ = 0.00065, $(^{36}Ar/^{37}Ar)_{Ca}$ = 0.000264, and $(^{40}Ar/^{39}Ar)_{K}$ = 0.0085; based on analyzes of Ca and K salts. Results were corrected for ^{37}Ar decay, and neutron-induced interference reactions. The irradiated slabs were loaded into an ultra-high vacuum system and mounted on a New Wave Research UP-213 stage. A 1064 nm IR CW fibre laser was focused into the sample chamber and was used to date spot in individual minerals in each of the sample slabs. This was achieved by using an automated shutter to allow the laser to couple with the sample for 20 ms, achieving a laser pit size of *ca.* 50μm. Each individual laser pit yielded an age for the mineral. After each laser spot the extracted gases were cleaned for 5 minutes using two SAES AP- 10

getters running at 450°C and room temperature. The gas clean-up and inlet system is fully automated and the mass spectrometer used was an MAP 215-50, which was operated by Labiew software. The mass discrimination value for atmospheric $^{40}Ar/^{36}Ar$ was measured at 285. Isotopes of ^{36}Ar to ^{40}Ar were measured 15 times per scan, and for 10 scans, the final measurements are extrapolations back to the inlet time. All data corrections were carried out using an Excel macro and the probability density plots and mean ages were calculated using Isoplot 3 (Ludwig, 2003). All ages are reported at the 2σ level and include a 0.5% error on the J value.

4. Results

4.1. Sampling

Ninety paragneiss samples were prepared and examined using standard optical microscopy to determine the textures, mineral contents, and rock types of each sample. Based on petrographic observations forty-one fresh samples were chosen for petrography, mineral chemistry, whole-rock major, trace and rare earth elements, and ^{40}Ar-^{39}Ar dating on biotite.

4.2. Rocks types and their textures

The Devrekani Massif is mostly composed of gneisses and metacarbonates, with lesser amphibolites (Fig. 2), which are cut by aplite, granite and tourmaline-bearing pegmatite veins. In the massif, gneissic and amphibolitic rocks form the lower parts and calcite marbles form the upper parts (Fig. 3a). Gneisses are both para- and ortho-gneisses and they are associated with amphibolites (Figs. 3b,c) that are discontinuous thin layers and small pod-like lenses. Any weakly- or non-foliated rocks are rich in quartz and feldspar minerals whereas sillimanite- and biotite-rich rocks have a distinct gneissic banding (Figs. 3d,e,f), and, strongly tectonized samples have localized migmatitic textures. Aplite and tourmaline-bearing

pegmatite veins cross-cut the Devrekani Massif, and consist of quartz, orthoclase, white mica and tourmaline. The paragneisses are generally grayish and light colored.

The paragneisses include a variety of lithologies with variable mineral contents and with lepidograno-, fibrolepidograno- and porphyro-blastic textures. The rocks generally consist of feldspar, quartz, biotite, garnet, cordierite, sillimanite and hercynite with minor Fe-Ti oxide (Table 1). Zircon and apatite are also present as accessory minerals, and muscovite, sericite and chlorite are secondary phases in assemblages. Generally, the paragneisses can be classified into five major groups based on mineral abundances: sillimanite-biotite (SB), garnet-biotite (GB), cordierite-biotite (CB), sillimanite-cordierite-biotite (SCB) and garnet-sillimanite-cordierite-biotite (GSCB) gneisses.

SB gneisses are weakly foliated and contain quartz (45-50%), K-feldspar (28-30%), biotite (10-12%), sillimanite (5-7%), and minor opaque minerals (1-2%), with secondary muscovite and accessory zircon. They are fine- to medium-grained with a fibrolepidogranoblastic texture. Biotite forms continuous foliation planes and sillimanite grains appear to be oriented prisms in contact with biotite, quartz and/or feldspar. Sillimanite is fine-grained and fibrolitic with an acicular fabric. Secondary muscovite forms small laths in veins and feldspar is sericitized.

GB gneisses contain quartz (25-27%), plagioclase (20-22%), K-feldspar (18-20%), biotite (12-15%), garnet (7-8%), minor sillimanite (3-4%) and opaque minerals (2-3%), with accessory zircon and apatite. They are generally banded; light domains contain quartz and feldspar, and dark domains are dominated by mafic minerals such as biotite. Their common texture is lepidoporphyroblastic with K-feldspar up to 2 mm and garnet porphyroblasts up to 0.9 mm (Fig. 4a). Most garnet porphyroblasts are surrounded by biotite flakes, some occur as rounded and tabular grains, and contain abundant inclusions of biotite, plagioclase, quartz, sillimanite and ilmenite. Inclusions in some garnet porphyroblasts are rotated, indicative of

syntectonic deformation and progressive metamorphism. Sillimanite crystals are typically elongated and needle-like fibroblasts and are associated with garnet and biotite.

CB gneisses are well-foliated paragneisses and the most common mineral assemblage is: quartz (25-30%), biotite (15-18%), K-feldspar (15-20%), plagioclase (10-15%), cordierite (8-10%), opaque minerals (3-5%), and minor sillimanite (2-4%) and hercynite (0-1%), with accessory zircon. They are generally fine- to medium-grained and have lepidogranoblastic and porphyroblastic textures with cordierite porphyroblasts up to 2.5 mm across. Cordierite forms subhedral to anhedral grains, commonly with inclusions of sillimanite and hercynite, and in some samples there is near-complete pinitization. The hercynite inclusions are worm-shaped green and dark green lamellae.

SCB gneisses have different mineralogical and textural properties that vary from sample to sample. However, the most abundant minerals are: quartz (28-32%), biotite (16-25%), cordierite (15-22%), plagioclase (8-13%), sillimanite (5-12%), K-feldspar (5-8%), and opaque minerals (2-4%), such as ilmenite, minor hercynite (0-1%), with accessory zircon. Common textures are fibro- and lepido-porphyroblastic with cordierite porphyroblasts (up to 3.5 mm). The gneissic texture in these rocks is well-developed and defined by the alignment of intergrown cordierite, biotite and sillimanite (Figs. 4c,d). These intergrowths suggest that sillimanite and biotite have been partly replaced by cordierite, which is locally heavily pinitized (Fig. 4e). Small zircon grains and some cordierite porphyroblasts have pleochroic halos. In some sillimanite-rich samples, a relative abundance of sillimanite is negatively correlated with cordierite. In some samples, sillimanite is well-developed, fibrous in form, and in equilibrium with biotite and cordierite in the rock matrix. This suggests that sillimanite crystallized either from anatectic melt or resulted from melt reactions.

GSCB gneisses are the most common rock type and consist mainly of quartz (27-33%), biotite (18-23%), plagioclase (10-18%), cordierite (9-15%), K-feldspar (8-13%), sillimanite

(4-12%), garnet (2-7%), hercynite (0-3%) and opaque minerals (2-4%), with accessory zircon. The foliation is well-developed and defined by the alignment of biotite, sillimanite and cordierite with the biotite-rich foliation surrounding porphyroblasts. These fine- to medium-grained rocks generally have granoblastic to fibro- and lepido-porphyroblastic textures with porphyroblasts of cordierite up to 3 mm and garnet up to 2 mm in diameter. These are mostly poikiloblastic with inclusions of quartz, biotite, sillimanite, hercynite and ilmenite. Most cordierites are pinitized and have pleochroic halos as do some more zircon grains. Garnet porphyroblasts are subhedral to anhedral, are often fractured and fragmented, and some appear as inclusions in cordierite (Figs. 4f,g). In some samples, euhedral garnets are partially or completely enveloped by coarse anhedral cordierite (Fig. 4h), suggesting that these garnet grains have been partly replaced by hercynite and cordierite (with hercynite occurring as worm-shaped forms inside the cordierite; see Fig. 4b).

4.3. Mineral chemistry

Mineral chemistry was obtained on garnet, biotite, K-feldspar, plagioclase, cordierite, sillimanite, hercynite and Fe-Ti oxides from selected gneisses to establish their mineral compositions and to enable the calculations of pressure and temperature conditions. Representative analyzes are found in supplementary Table S1.

Garnets vary in size and composition. The size of crystals ranges from 0.5 to 2 mm (type-I), whereas the smaller porphyroblasts are 0.02-0.5 mm (type-II). Type-I crystals are anhedral to subhedral in form and are mostly fractured. The large porphyroblasts frequently contain isolated grains of Ti-rich biotite (2.94-4.72 wt% TiO_2), quartz, plagioclase, fibrous sillimanite and opaque mineral such as ilmenite (Fig. 5). Type-II crystals occur both as subhedral to euhedral phenocrysts and some of them have porphyroblastic textures. There is no core-rim chemical zoning and there are only minor compositional variations between grains. Garnets

are rich in almandine with Alm+Sps (72-92%), the andradite and uvarovite end-members are in low concentrations (<4%). The pyrope component in some samples is relatively high, ranging from 5 to 23%. The range of the composition of Type-I garnets is $Alm_{66-80}Grs_{0-3}Prp_{5-10}And_{0-4}Sps_{10-24}$ [$(Mg/(Mg+Fe^{2+}) = 0.1-0.3)$], whereas Type-II garnets have a range of the composition of $Alm_{43-60}Grs_{0-18}Prp_{6-23}And_{0-3}Sps_{13-33}$ [$(Mg/(Mg+Fe^{2+})= 0.07-0.13)$].

Biotite flakes occur parallel to the foliation planes along with sillimanite and cordierite. They are relatively Fe-rich with [$(Fe^{2+}/(Fe^{2+}+Mg)$] ratio of 0.39-0.67 and moderate Al^{VI} contents (0.5-1.1 apfu), corresponding to siderophyllite component enrichment with X_{Phl} [$(Mg/(Fe^{2+}+Mg+Mn+Al^{VI})$] ratio of 0.28-0.57. Additionally, TiO_2 in biotite varies from 1.81 to 4.72 wt%. In some paragneisses, biotites occur as inclusions in coarse-grained garnet and cordierite porphyroblasts, suggesting that they more likely to be a component of a prograde metamorphic reaction.

Plagioclases occur as fine to coarse-grained phenocrysts, they are subhedral to anhedral, with some that are fragmented, and all are partly sericitized. The twinning is generally albite in form and the compositions range from oligoclase to andesine with An_{18-35} (Fig. 6a).

*K-feldspar*s are medium- to fine-grained and often occur as aggregates parallel to the foliation. The chemical composition is relatively homogeneous and mostly orthoclase ($An_{0-1}Ab_{4-26}Or_{73-96}$; Fig. 6a).

Cordierites are present as subhedral to anhedral coarse-grained aggregates, with porphyroblastic and/or poikiloblastic textures. They have *ca.* 100 wt% EMP totals indicating that fluid species such as H_2O or CO_2 are absent in the crystal structure. The $Mg/(Mg+Fe^{2+})$ ratio ranges between 0.48 and 0.71, and the CaO and K_2O contents are generally low (<0.17 wt%). The contents of MnO and Na_2O vary between 0.30-1.09 wt% and 0.13-0.37 wt%, respectively.

Hercynites are present as inclusions within cordierite. Hercynite contains 56-62 wt% Al_2O_3 and 24-36 wt% FeO^T, and $Mg/(Mg+Fe^{2+})$ ratios vary from 0.09 to 0.11 (Fig. 6b). These samples have low Cr_2O_3 (0.11-0.62 wt%) with Cr/(Cr+Al) values ranging from 0.001 to 0.007 and the calculated formula is $Fe^{2+}_{0.90\text{-}0.95}Mg_{0.05\text{-}0.1}Al_{2.00}O_4$. In some samples, aggregates occur in cordierite coronas as a reaction product between sillimanite and garnet porphyroblast, a texture that suggests a stage of decompression and cooling.

4.4. ^{40}Ar-^{39}Ar dating

The results of the ^{40}Ar-^{39}Ar dating are available as supplementary material in Table S2. A summary of ages is provided in Table 2, and age data are plotted in Fig. 7. Individual ^{40}Ar-^{39}Ar ages of GCSB gneiss sample H3 range from 225±3 to 166±3 Ma (n= 9). However, there are two groups of ages when plotted against $^{38}Ar_{Cl}/^{39}Ar_K$ (Fig. 7a). The weighted mean of 5 ages (group-I) is 174±6 Ma (Aalenian), and the second group has a range of 225±3 - 202±3 Ma (group-II, n=4). This indicates that two groups are distinct in terms of age and in argon isotope composition, and, therefore, it is likely that an older biotite has been partially reset by a subsequent thermal event. Individual biotite ages of GB gneiss KD1 range from 164±4 to 152±1 Ma (n=10). There is a cluster at 160-155 Ma (n=7) and the weighted mean age is 158±1 Ma (Oxfordian; Fig. 7b). In SCB gneiss sample KD7B, individual ages range from 173±3 to 139±6 Ma (n=9). The weighted mean age is not meaningful because of the very high MSWD value (age of 156±8 Ma; Fig. 7c). The measured biotite ^{40}Ar-^{39}Ar average ages from the H3, KD1 and KD7B samples range between *ca.* 156 and 174 Ma. These age data indicate that the rocks cooled to 300-350°C during the Middle-Upper Jurassic, which is the mostly accepted closure temperature for ^{40}Ar-^{39}Ar in biotite (Harrison et al., 1985; Grove and Harrison, 1996).

4.5. Whole-rock geochemistry

The whole-rock geochemical data are plotted on diagrams that can be used to determine the provenance and tectonic setting of the protoliths. The representative analyzes are given as supplementary material in Table S3. LOI values are generally low (1-3 wt%) and suggest that the selected samples are fresh. The rocks have high Al_2O_3 (12-21 wt%) and $Fe_2O_3^T$ (7-11 wt%), and low MgO (1.88-3.52 wt%; Mg# = 0.36-0.51) contents. Additionally, CaO, Na_2O and K_2O vary between 0.32-2.13 wt%, 0.89-2.49 wt% and 2.03-3.93 wt%, respectively. This compositional range may be due to variations in protolith composition, or metamorphic conditions, and therefore, less mobile elements such as Zr, Ti, Ni Th, Sc and REE were used for classifying the protolith composition (e.g., Pearce, 1983; Winchester, 1984; Rollinson, 1993). The paragneisses have high Ni contents and intermediate Zr/TiO_2 ratios - the $100*TiO_2/Zr=0.4$ (wt%/ppm) empirical discrimination ratio (Garcia et al., 1991) is in the range 0.42-0.78. The samples also have low $\log(SiO_2/Al_2O_3)$ and slightly high $\log(Fe_2O_3^T/K_2O)$ ratios. Th/Sc ratios of the samples vary between 0.5-0.8 and have relatively high La contents.

Mid-ocean ridge basalt (MORB) and Post-Archaean average Australian sedimentary rock (PAAS)-normalized trace element diagrams with chondrite and PAAS-normalized REE diagrams are used to identify the source characteristics of the paragneisses. They are also compared with North American shale composite (NASC) of Gromet et al. (1984) and the upper crust (UC) compositions suggested by Taylor and McLennan (1981). The large-ion lithophile elements (LILE), Sr, Rb, Ba, Th and K, are generally enriched; in contrast, the high field strength elements (HFSE), Ta, Nb, Ti and P, are depleted (Fig. 8a). Zr, Hf, Sm, Y and Yb concentrations are close to MORB. The negative Nb, Ta and Ti anomaly, with high Th/Ta ratios (11-25), confirms their formation in a subduction zone environment (Pearce, 1983; Rogers and Hawkesworth, 1989; Gorton and Schandl, 2000). The high LILE contents may

also indicate a crustal contribution. In Fig. 8b, the trace elements are normalized to PAAS which demonstrates that they are approximate to PAAS with positive Nb and negative Cu anomalies. The significant positive Nb anomaly indicates the presence of titanite minerals in the protoliths.

Chondrite-normalized REE patterns (Fig. 8c) are typically concave upwards with La_N/Lu_N= 3.70-10.75 and La_N/Yb_N averaging 7.33. Paragneiss samples have La_N/Sm_N= 2.96-3.88 and Gd_N/Lu_N= 0.98-1.74. The REE patterns also show Eu anomalies ranging from 0.47 to 1.27, suggesting plagioclase fractionation, or crustal contribution, and the LREE enrichment with negative Eu anomalies indicates a continental provenance. Representative PAAS-normalized REE data are shown in Fig. 8d, where samples plot close to PAAS and are similar in composition to shale. The distribution of the REE patterns indicates that their protoliths might have been sediments, of predominantly shale composition, and implies that sedimentary protoliths were derived from a mafic and/or intermediate source.

4.6. Metamorphic reactions in the paragneisses

The Devrekani paragneisses have resulted from transitional upper amphibolite to lower granulite facies metamorphism of sedimentary protoliths. Common mineral assemblages are presented in Fig. 2 and Table 1.

4.6.1. Sillimanite-bearing gneisses

In these samples primary muscovite is absent and sillimanite appears to be oriented and fibrous, and in contact with biotite, quartz and/or K-feldspar. The assemblage Sil+Kfs indicates that the temperature was above *ca.* 700°C within the sillimanite stability field. Therefore, in the K_2O-Al_2O_3-SiO_2-H_2O (KASH) system, dehydration reaction producing Sil + Kfs as follows:

$$Ms + Qz = Sil + Kfs + H_2O \text{ (or Lq)} \quad (1)$$

This reaction is regarded as the lower boundary of the upper sillimanite zone of the amphibolite facies (Yardley, 1990). The textures in this rock suggest that Qz + Pl + Kfs + Bt + Sil (+H_2O) was a stable assemblage, suggesting that the muscovite dehydration melting reaction (1) modified by Spear et al. (1999) resulted in the growth of plagioclase:

$$Ms + Qz + Pl = Sil + Kfs + Lq \quad (2)$$

4.6.2. Cordierite-bearing gneisses

Garnet is not present in most cordierite-bearing gneisses, and Crd + Kfs is in equilibrium, indicating that garnet was completely consumed by the cordierite-producing reactions. Most samples are characterized by Crd + Bt + Sil + Kfs + Qz with minor hercynite and they are likely to have formed through the reaction (3):

$$Sil + Bt + Qz = Crd + Kfs + Lq \quad (3)$$

Where garnet is present it is as inclusions within cordierite, and along with fibrolitic sillimanite inclusions. It is likely that another reaction also contributed to the production of cordierite:

$$Grt\ (Alm) + Sil + Qz + H_2O = Crd \quad (4)$$

4.6.3. Garnet, cordierite and hercynite-bearing gneisses

Cordierite and hercynite are present in some garnet-bearing rocks, hercynite is generally observed in cordierite porphyroblast cores. The occurrence of anhedral remnant garnet as inclusions in some cordierite porphyroblasts, and fibrolitic sillimanite associated with hercynite within cordierite, suggests that hercynite was formed by the reaction:

$$Sil + Grt (+ Qz + Kfs + Lq) = Crd + Hc \quad (5)$$

Where garnet occurs as subhedral and/or anhedral grains it has variable mineral inclusions, such as biotite, sillimanite, quartz, plagioclase and ilmenite, where the abundance of biotite and quartz are negatively correlated with cordierite and garnet. Most cordierite grains include fibrolitic sillimanite as inclusions. The textural observations in these rocks suggest that cordierite, garnet and K-feldspar were produced by the consumption of sillimanite, biotite, quartz and plagioclase by the reaction:

$$Sil + Bt + Qz + Pl = Crd + Grt + Kfs + Lq \quad (6)$$

Overall, the assemblage of biotite, garnet, cordierite, K-feldspar, quartz and plagioclase, with hercynite and fibrolitic sillimanite as inclusions in cordierite, is the highest-grade assemblage from the Devrekani Massif rocks. The prograde evolution of the paragneisses included sillimanite zone conditions in the amphibolite facies passing up into the cordierite-garnet-K-feldspar zone of the lower granulite facies.

5. Discussion

5.1. P-T estimates of metamorphism

Peak *P–T* conditions for the Devrekani paragneisses were estimated using the GeoThermoBarometry computer software (GTB v2.1, 2006) based on mineral assemblages and compositions from the *GB*, *CB*, *SCB* and *GSCB* gneisses.

The Na-in-cordierite (Na-in-Crd) thermometer is applied because cordierite is a major component in most samples. For comparison, it is also applied garnet-biotite (Grt-Bt) and garnet-cordierite (Grt-Crd) Fe-Mg exchange thermometers. Detailed temperature estimates are presented as supplementary in Table S4 and summarized in Table 3. The Na-in-Crd geothermometer of Mirwald (1986) is used since it can be applied to natural cordierite coexisting with Pl + Kfs + Bt + Qz (Kalt et al., 1998). The Na (cpfu) content of cordierite varies from 0.025 to 0.065 with a mean of 0.039, resulting in temperature estimates of 698-808°C with a mean of 770°C (Table 3 and supplementary Table S4). Other temperature estimates for the GB and GSCB gneisses were calculated using the Fe-Mg exchange method of Ferry and Spear (1987) applied to matrix biotite and garnet porphyroblasts. The average temperatures range from 619±32°C to 822±20°C at an assumed 6 kbar (Table 3 and supplementary Table S4), corresponding to the average results from the GASP and GRIPS barometers. The homogeneity of garnet and the presence of high-temperature mineral inclusions, suggest that these estimates of peak *P-T* conditions may be appropriate. The Fe-Mg geothermometer of Bhattacharya et al. (1988), which is based on the exchange of Fe and Mg between Grt-Crd couples, yeilded temperatures from 646 to 732°C at an assumed pressure of 6 kbar (supplementary Table S4). Overall, the average temperature values vary from 653±5°C to 709±22°C (Table 3) and are consistent with the mineral paragenesis and textural observations.

The geobarometry is based on the garnet-sillimanite-quartz-plagioclase (GASP), garnet-rutile-ilmenite-plagioclase-quartz (GRIPS) and garnet-rutile-sillimanite-ilmenite-quartz (GRAIL) barometers. GASP and GRIPS yielded consistent pressures of 5 to 7 kbar at 750 and 800°C respectively, however, pressures derived from the GRAIL barometer for samples are relatively high and range from 7.5 to 8.6 kbar (Table 4). Pressures determined from equilibria involving Crd + Hc are relatively low (~4 kbar), and consistent with the observed mineral parageneses and textural properties (see Figs. 4 and 9). The isopleths derived from the GASP barometer dissect the curve of reaction (6) at ~750°C and ~4.75 kbar. The intersections of the Na-in-Crd geothermometer (~750-800°C) with the GASP isopleths yielded pressure estimates of 4.75-7.25 kbar for paragneissic rocks with an aluminosilicate phase. Combining the mineral assemblages, textural features, compositions and the geothermobarometry indicates that peak *P–T* conditions were 6±1 kbar and 775±25°C (Fig. 9).

5.2. Potential protoliths of the paragneisses

Gneisses produced by high-grade metamorphic conditions can occur in various geological environments, such as continental orogenic belts. The geochemical characteristics of the metamorphic rocks provide information about their source material. According to mineralogical observations and whole-rock geochemical data the possible protoliths for the studied paragneisses are shales and wackes, indicating a pelitic sediment source (Figs. 10a,b). In the provenance discrimination diagram of Roser and Korsch (1988), the paragneiss samples reflect an intermediate igneous provenance (Fig. 10c). Also, on the Th vs Sc discrimination diagram of McLennan et al. (1993), the samples indicate intermediate and mafic sources (Fig. 10d). Based on the La vs. Th diagram of Taylor and McLennan (1985), the paragneiss samples fall into the post-Archean field (Fig. 10e). Plotting data on the discrimination diagram of Roser and Korsch (1986) reveals that the protolith might have been

deposited in an active continental and a passive margin setting (Fig. 10f). The distribution and concentrations of REE and trace elements, along with the negative Ta, Nb, P and Ti anomalies, as well as the high Th/Ta, emphasizes that the protoliths were subduction-related (Pearce, 1983; Rogers and Hawkesworth, 1989; Gorton and Schandl, 2000) and close to the average composition of the PAAS and NASC sedimentary rocks. Moreover, significant LREE enrichment along with ΣLREE/ΣHREE (4.63-9.57) and Th/Sc (0.5-0.8) ratios suggests that the protoliths were derived from a mafic and/or intermediate sources. According to our new, and existing, petrological and geochronological data, most protoliths of the paragneiss rocks in the Devrekani Massif were originally sediments that were predominantly deposited during the pre-Jurassic period, and fed by Permo-Carboniferous magmatic rocks (Duru et al., 2004; Nzegge, 2008; Okay et al., 2014; Gücer, 2014; Gücer et al., 2016; Okay et al., 2017; Okay and Topuz, 2017; this study; Table 2).

5.3. Geodynamic implications

The petrochemical and geochronological results reported here for the Jurassic metamorphic rocks enable a re-assessment of the geodynamic evolution of the Central Pontides, in which there are oceanic subduction–accretion complexes, magmatic arcs and fore-arc sequences formed during the Triassic, Jurassic and Cretaceous (Akdoğan et al., 2017; Okay et al., 2017, Çimen et al., 2018). The presence of the Jurassic subduction–accretion complexes along with the subduction zone ophiolites (Göçmengil et al., 2013; Topuz et al., 2013a,b), and the existence of Jurassic ophiolitic rocks in the Late Cretaceous mélanges, suggest that the subduction zone system was active during the Early to Middle Jurassic period (e.g., Dilek and Thy, 2006; Sarıfakıoğlu et al., 2009; Çelik et al., 2011; Gücer and Aslan, 2014).

Zircon U-Pb ages from the orthogneisses in the Devrekani Massif yielded ages of 253±9, 268±5 and 316±9 Ma (Gücer et al., 2016), indicating that the orthogneiss protoliths developed during the Permo-Carboniferous period. The Variscan terranes in the Central Pontides are represented by medium- to high-grade metamorphic rocks consisting predominantly of orthogneisses, paragneisses, amphibolites and meta-ultramafic rocks. In addition, Permo-Carboniferous magmatism is a common feature of the Variscan basement units (Duru et al., 2004; Okay et al., 2006; Nzegge, 2008). Apart from these magmatic ages, the ^{40}Ar-^{39}Ar biotite and K-Ar hornblende cooling ages range from the Sinemurian to Kimmeridgian (e.g., Nzegge, 2008; Okay et al., 2014; Gücer, 2014; Gücer et al., 2016; this study). In particular, the ^{40}Ar-^{39}Ar biotite ages are Middle-Late Jurassic (Fig. 11), so it is highly likely that these metamorphic rocks finally cooled to below *ca.* 300°C during the Late Jurassic.

Okay et al. (2014) suggested that there was no crustal thickening in the Central Pontides, prior to the Early-Middle Jurassic extension and metamorphism, based on the regional stratigraphy and petrography of the metamorphic rocks. In this model, the Jurassic magmatism and metamorphism in the region occurred simultaneously with submarine sedimentation and volcanism in an extensional magmatic arc setting. Similar Jurassic arc-type volcanic rocks were also reported from the Eastern Pontides (e.g., Dokuz et al., 2017; Karslı et al., 2017), Crimea (e.g., Meijers et al., 2010) and Caucasus (e.g., Sosson et al., 2010). The Central Pontides are generally characterized by the presence of Jurassic–Cretaceous subduction–accretion complexes in the south, and mid-Cretaceous submarine turbidites in the north (e.g., Okay et al., 2013, 2017; Aygül et al., 2016; Akdoğan et al., 2017). From these, the Jurassic accretionary complex is represented by the Küre unit, that may have been deposited in a fore-arc basin (Okay et al., 2015). Similar accretionary prisms are known in the Crimea and Caucasus as the Tauric Group (Meijers et al., 2010) and the Dizi Series (Adamia et al.,

2011), respectively. All these complexes may represent the accretionary prisms of the northward subducting ocean beneath the accreted southern margin of Laurasia.

Based on the new petrological data and associated field relations, the following tectonic model is proposed for the Jurassic metamorphism during the continental extension in the region (Fig. 12). The calc-alkaline arc granitoid magmatism resulted from the northward subduction of the Paleo-Tethyan oceanic crust during the Permo-Carboniferous. Later, the Triassic-Jurassic accretionary prism (Küre Complex) could have been deposited by continuing northward Paleo-Tethyan subduction beneath the basement units of the Central Pontides. At the same time, the Devrekani Massif may have been metamorphosed within an extensional magmatic arc setting as proposed by Okay et al. (2014). Here, the high-temperature area formed in mid-lower crust at about 20 km depth due to the extension of the Laurasia continent. Therefore, the volcano-sedimentary protoliths of the paragneisses and the granitic protoliths of the orthogneisses were metamorphosed under high-temperature conditions. Following the Jurassic period, the Devrekani Massif was not subjected to progressive regional metamorphism and the Early Cretaceous subduction–accretion prism continued to form in the southern Central Pontides.

6. Conclusions

The Devrekani Massif in the Northern Turkey is important for understanding the metamorphic processes and geodynamic evolution of the Central Pontides. This study reports new petrological, petrochemical and ^{40}Ar-^{39}Ar radiometric age data from the Devrekani paragneisses, and provides new constraints on the timing of the metamorphism. The main results can be summarized as follows:

- There are five main types of paragneisses with the diagnostic mineral assemblage of quartz, K-feldspar ($An_{0-1}Ab_{4-26}Or_{73-96}$), plagioclase ($An_{18-35}$), biotite [($X_{Phl}$: 0.28-0.57;

Mg/(Mg+Fe^{2+}): 0.33-0.61)], sillimanite, cordierite [(Mg/(Mg+Fe^{2+}): 0.48-0.71)], garnet ($Alm_{43-80}Grs_{0-18}Prp_{5-23}And_{0-4}Sps_{10-33}$) and hercynite. The mineral assemblages of the paragneisses, determined here, indicate that the prograde history passed from sillimanite zone conditions in the amphibolite facies up to cordierite-garnet-K-feldspar zone conditions in the granulite facies.

- Whole-rock geochemistry of paragneisses reveals that the protoliths were pelitic sediments such as shales and greywackes. The major and trace elements indicate intermediate and mafic igneous provenances, deposited in both an active continental margin and a passive margin setting. In general, LILE and LREE are enriched, whilst HFSE are depleted in samples, with negative Eu anomalies. The compositions of the protoliths are close to the average composition of the PAAS and NASC sedimentary rocks.
- The petrological and geochronological data suggest that the protoliths are related to multiple sources, and linked to pre-Jurassic sedimentation and continental arc magmatism, overprinted by Jurassic metamorphism. It is most likely that peak metamorphism was during the Middle–Upper Jurassic period (*ca.* 174–156 Ma), suggesting that the metamorphic rocks cooled below 300°C at *ca.* 156 Ma.
- Temperatures for peak metamorphism range from 646 to 822°C at 6 kbar. GASP and GRIPS barometry yielded consistent pressures of 5.4 to 7.3 kbar at 750 to 800°C respectively. The estimated peak *P–T* conditions of metamorphism are 6±1 kbar and 775±25°C.
- The Jurassic H*T* metamorphism developed within a continental crust, in the deep segments of an extensional continental arc that developed on the Laurasian southern margin, due to the northward subduction of Paleo-Tethyan oceanic lithosphere.

Acknowledgments

This work was financially supported by the Karadeniz Technical University, Scientific Research Fund (BAP Project no: 8702). The authors sincerely thank İrfan Temizel, Emel Abdioğlu Yazar and Cem Yücel for their help during the field and laboratory studies. Many thanks also go to H.J. Bernhardt for performing the electron probe microanalysis, and to James Malley for assistance with ^{40}Ar-^{39}Ar analysis. We would like to thank Fraukje M. Brouwer and an anonymous reviewer for their critical comments and suggestions, which improved the quality of the paper. We are also grateful to editorial handling of İbrahim Uysal and Mei-Fu Zhou for their constructive and helpful feedback, and timely processing of the manuscript.

References

Adamia, S., Zakariadze, G., Chkhotua, T., Sadradze, N., Tsereteli, N., Chabukiani, A., Gventsadze, A., 2011. Geology of the Caucasus: A review. Turk J Earth Sci 20, 489–544.

Akdoğan, R., Okay, A.I., Sunal, G., Tari, G., Meinhold, G., Kylander, A.R.C. 2017. Provenance of a large Lower Cretaceous turbidite submarine fan complex on the active Laurasian margin: Central Pontides, northern Turkey. J Asian Earth Sci 134, 309-329.

Akmaz R.M., Uysal I. and Saka S., 2014. Compositional variations of chromite and solid inclusions in ophiolitic chromitites from the southeastern Turkey: Implications for chromitite genesis. Ore Geol Rev 58, 208–224.

Aldanmaz E., Yalınız M.K., Güçtekin A., Göncüoğlu M.C., 2008. Geochemical characteristics of mafic lavas from the Tethyan ophiolites in western Turkey: implications for heterogeneous source contribution during variable stages of ocean crust generation. Geol Mag 145, 37-54.

Altun, İ.E., Şengün, M., Keskin, H., Akçaören, F., Sevin, M., Deveciler, E., Akat, M.U., 1990. Geological map series of Turkey, Kastamonu-B17 quadrangle: Turkey MTA (Mineral Research & Exploration General Directorate), scale 1:100 000, 1 sheet.

Atalay, İ., 1987. Introduction to geomorphology of Turkey (in Turkish): İzmir, Ege University publications, 234 pp.

Aygül, M., Okay, A.I., Oberhänsli, R., Sudo, M. 2016. Pre-collisional accretionary growth of the southern Laurasian active margin, Central Pontides, Turkey. Tectonophysics 671, 218-234.

Aysal, N., Şahin, S.Y., Güngör, Y., Peytcheva, I., Öngen, S. 2018. Middle Permian–early Triassic magmatism in the Western Pontides, NW Turkey: Geodynamic significance for the evolution of the Paleo-Tethys. J Asian Earth Sci 164, 83-103.

Aysal, N., Ustaömer, T., Öngen, S., Keskin, M., Köksal, S., Peytcheva, I., Fanning, M. 2012. Origin of the Early-Middle Devonian magmatism in the Sakarya Zone, NW Turkey: Geochronology, geochemistry and isotope systematics. . J Asian Earth Sci 45, 201-222.

Bhattacharya, A., Mazumdar, A.C., Sen, S.K., 1988. Fe-Mg mixing in cordierite: constraints from natural data and implications for cordierite-garnet geothermometry in granulites. Am Mineral 73, 338-344.

Bohlen, S.R., Liotta, J.J., 1986. A barometer for garnet amphibolites and garnet granulites, J Petrol 27, 1025-1034.

Bohlen, S.R., Wall, V.J., Boettcher, A.L., 1983b. Experimental investigations and geological applications of equilibria in the system: FeO-TiO_2-Al_2O_3-SiO_2-H_2O. Am Mineral 68, 1049-1058.

Boynton, W.V., 1984. Cosmochemistry of the rare earth elements; meteorite studies, in: Henderson, P. (Eds.), Rare earth element geochemistry: Elsevier Science Publishing Co., Amsterdam, pp. 63-114.

Çelik, Ö.F., Marzolli, A., Marschik, R., Chiaradia, M., Neubauer, F., Öz, I., 2011. Early-Middle Jurassic intra-oceanic subduction in the İzmir-Ankara-Erzincan Ocean, Northern Turkey. Tectonophysics 509, 120-134.

Chen, F., Siebel, W., Satır, M., Terzioğlu, N., Saka, K., 2002. Geochronology of the Karadere basement (NW Turkey) and implications for the geological evolution of the İstanbul Zone. Int J Earth Sci 91, 469-481.

Çimen, O., Göncüoğlu, M. C., Simonetti, A., Sayıt, K., 2018. New zircon U-Pb LA-ICP-MS ages and Hf isotope data from the Central Pontides (Turkey): Geological and geodynamic constraints. J Geodyn 116, 23-36.

Çimen, O., Göncüoğlu, M.C., Sayıt, K., 2016. Geochemistry of the metavolcanic rocks from the Çangaldağ Complex in the Central Pontides: implications for the Middle Jurassic arc-back-arc system in the Neotethyan Intra-Pontide Ocean. Turk J Earth Sci 25, 491-512.

Çimen, O., Göncüoğlu, M.C., Simonetti, A., Sayıt, K., 2017. Whole rock geochemistry, Zircon U-Pb and Hf isotope systematics of the Çangaldağ Pluton: Evidences for Middle Jurassic Continental Arc Magmatism in the Central Pontides, Turkey. Lithos 290-291, 136-158.

Çimen, O., Öztüfekçi-Önal, A. 2018. Preliminary geochemical data of the mafic rocks from the Ovacik and Pülümür Ophiolite Zone (Eastern Anatolia, Turkey): Implications for the geodynamic evolution of the northern Neotethyan Ocean. Ofioliti 43(2), 103-116.

Dean, W.T., Martin, F., Monod, O., Demir, O., Rickards, A.B., Boltynck, P., Bozdoğan, N., 1997. Lower Paleozoic stratigraphy, Karadere-Zirze area, Central Pontides, northern Turkey. Geol Mag 137, 555-582.

Dilek, Y., Thy, P., 2006. Age and petrogenesis of plagiogranite intrusions in the Ankara Melange, Central Turkey. Isl Arc 15, 44-57.

Dokuz, A., Aydınçakır, E., Kandemir, R., Karslı, O., Siebel, W., Derman, A.M., Turan, M., 2017. Late Jurassic magmatism and stratigraphy in the Eastern Sakarya zone,Turkey: evidence for the slab Breakoff of paleotethyan oceanic lithosphere. J Geol 125, 1–31.

Duru, M., Pehlivan, Ş., Şentürk, Y., Yavaş, F., Kar, H., 2004. New results on the lithostratigrapy of the Kazdağ Massif in nortwest Turkey. Turk J Earth Sci, A special issue commemorating, Tekeli, O., pp. 177-186.

Ferry, J.M., Spear, F.S., 1978. Experimental calibration of the partitioning of Fe and Mg between biotite and garnet. Contrib Mineral Petrol 66, 113-117.

Frassi, C., Marroni, M, Pandolfi, L, Göncüoğlu, M.C., Ellero, A., Ottria, G., Sayıt, K, Mcdonald, C.S., Balestrieri, M.L., Malasoma, A., 2017. Burial and exhumation history of the Daday Unit (Central Pontides, Turkey): implications for the closure of the Intra-Pontide oceanic basin. Geol Mag doi:10.1017/S0016756817000176.

Garcia, D., Coelho, J., Perrin, M., 1991. Fractionation between TiO_2 and Zr as a measure of sorting within shale and sandstone series (Northern Portugal). Eur J Mineral 3, 401-414.

Göçmengil, G., Altıntaş, İ.E., Topuz, G., Çelik, Ö.F., Özkan, M., 2013. Diverse tectonic settings of formation of the metaigneous rocks in the Jurassic metamorphic accretionary complexes (Refahiye, NE Turkey) and their geodynamic implications. Geodin Acta 26, 294-310.

Göncüoğlu, M. C., Kozlu, H., Dirik, K., 1997. Pre-Alpine and Alpine terranes in Turkey: explanatory notes to the terrane map of Turkey. Annales Géologiques des Pays Helleniques 37, 515-536.

Göncüoğlu, M.C., 2010. Introduction to the Geology of Turkey: Geodynamic evolution of the pre-Alpine and Alpine Terranes. Turkey MTA (Mineral Research & Exploration General Directorate) pp. 1-69.

Göncüoğlu, M.C., Marroni, M., Pandolfi, L., Ellero, A., Ottria, G., Catanzariti, R., Tekin, U.K., Sayıt, K., 2014. The Arkot Dağ Melange in Araç area, central Turkey: Evidence of its origin within the geodynamic evolution of the Intra-Pontide suture zone. J Asian Earth Sci 85, 117-139.

Gorton, M.P., Schandl, E.S., 2000. From continents to island arcs: a geochemical index of tectonic setting for arc-related and within-plate felsic to intermediate volcanic rocks. Can Mineral 38, 1065-1073.

Gromet, L.P., Dymek, R.F., Haskin, L.A., Korovet, R.L., 1984. The "North American Shale Composite": its compilation, major and trace element characteristics. Geochim Cosmochim Acta 48, 2469-2482.

Grove, M., Harrison, T.M., 1996. ^{40}Ar* diffusion in Fe-rich biotite: Am Mineral 81, 940-951.

Gücer, M.A., 2014. Petrochemistry, petrology and geochronology of the Devrekani (Kastamonu, Turkey) metamorphics, Ph.D. thesis (in Turkish with English abstract): Trabzon, Karadeniz Technical University, 276 pp.

Gücer, M.A., Arslan, M., Sherlock, S., Heaman, L.M., 2016. Permo-Carboniferous granitoids with Jurassic high temperature metamorphism in Central Pontides, Northern Turkey. Mineral Petrol 110, 943-964.

Gücer, M.A., Aslan, Z., 2014. ^{40}Ar-^{39}Ar age, petrography and geochemistry of the Yoncayolu Metamorphic Rocks (NE Turkey): Subduction-related metamorphism under greenschist facies conditions. Neues Jahrb Mineral Abh 191, 257-276.

Harrison, T.M., Duncan, I., McDougall, I., 1985. Diffusion of ^{40}Ar in biotite: temperature, pressure, and compositional effects. Geochim Cosmochim Acta 49, 2461-2468.

Herron, M.M., 1988. Geochemical classification of terrigeneous sands and shales from core or log data. J Sediment Petrol 58, 820-829.

Hippolyte, J.J., Espurt, N., Kaymakci, N., Sangu, E., Müller, C., 2016. Cross-sectional anatomy and geodynamic evolution of the Central Pontide orogenic belt (northern Turkey). Int J Earth Sci, 105, 81-106.

Kalt, A., Altherr, R., Ludwig, T., 1998. Contact metamorphism in pelitic rocks on the island of Kos (Greece, Eastern Aegean Sea): A test for the Na-in-cordierite thermometer. J Petrol 39, 663-688.

Karslı, O., Dokuz, A., Kandemir, R., 2017. Zircon Lu–Hf systematics and U–Pb geochronology, whole-rock Sr–Nd isotopes and geochemistry of the early Jurassic Gokcedere pluton, Sakarya Zone-NE Turkey: a magmatic response to roll-back of the PaleoTethyan oceanic lithosphere. Contrib Mineral Petrol 172, 1–27.

Koziol, A.M., 1989. Recalibration of the Garnet-Plagioclase-Al_2SiO_5-Quartz (GASP) geobarometer and applications to natural parageneses. Eos (Transactions of the American Geophysical Union) 70, 493.

Kozur, H., Aydın, M., Demir, O., Yakar, H., Göncüoğlu, M.C., Kuru F., 2000. New stratigraphic results from the Paleozoic and Early Mesozoic of the Middle Pontides (Northern Turkey). Geol Croatia 53, 209-268.

Le Breton, N., Thompson, A.B., 1988. Fluid-absent (dehydration) melting of biotite in metapelites in the early stages of crustal anataxis. Contrib Mineral Petrol 99, 226-237.

Ludwig, K.R., 2003. User's manual for Isoplot/Ex version 3.0: a geochronological toolkit for Microsoft Excel. Berkeley Geochronology Center Spec. Pub. No. 4, 70 p. Berkeley, California.

McCann, T., Chalot-Prat, F., Saintot, A., 2010. The Early Mesozoic evolution of the Western Greater Caucasus (Russia): Triassic-Jurassic sedimentary and magmatic history. Geol Soc London Spec Pub 340, 181–238.

McLennan, S.M., 1989. Rare earth elements in sedimentary rocks: influence of provenance and sedimentary processes, in: Lipin, B.R., MacKay, G.A. (Eds.), Geochemistry and Mineralogy of Rare Earth Elements: Mineralogical Society of America, pp. 169-200.

McLennan, S.M., Hemming, S., McDaniel, D.K., Hanson, G.N., 1993. Geochemical approaches to sedimentation, provenance and tectonics. Special Papers - Geol Soc Am 284, 21-40.

Meijers, M.J.M., Vrouwe, B., van Hinsbergen, D.J.J., 2010. Jurassic arc volcanism on Crimea (Ukraine): Implications for the paleo-subduction zone configuration of the Black Sea region. Lithos 119, 412–426.

Mirwald, P.W., 1986. Ist cordierit ein geothermometer?: Fortschritte der Mineralogie 64, 119.

Nzegge, O.M., 2008. Petrogenesis and geochronology of the Deliktaş, Sivrikaya and Devrekani granitoids and basement, Kastamonu Belt-Central Pontides (NW Turkey): Evidence for Late Palaeozoic-Mesozoic plutonism, and geodynamic interpretation, Ph.D. thesis: Deutschland, Institut für Geowissenschaften Universität Tübingen, 157 pp.

Okay, A.I., 2008. Geology of Turkey: A synopsis. Anschnitt 21, 19-42.

Okay, A.I., Altıner, D., Kılıç, A.M., 2015. Triassic limestone, turbidites and serpantinite the Cimmeride orogeny in the Central Pontides. Geol Mag 152, 460-479.

Okay, A.I., Altiner, D., Sunal, G., Aygül, M., Akdoğan, R., Altiner, S., Simmons, M., 2017. Geological evolution of the Central Pontides. Geol Soc London Spec Pub 464, doi: 10.1144/SP464.3.

Okay, A.I., Göncüoğlu, M.C., 2004. The Karakaya Complex: A review of data and concepts. Turk J Earth Sci 13, 77-95.

Okay, A.I., Sunal, G., Sherlock, S., Altıner, D., Tüysüz, O., Kylander-Clark, A.R.C., Aygül, M., 2013. Early Cretaceous sedimentation and orogeny on the southern active margin of Eurasia: Central Pontides, Turkey. Tectonics 32, 1247-1271.

Okay, A.I., Sunal, G., Tüysüz, O., Sherlock, S., Keskin, M., Kylander-Clark, A.R.C., 2014. Low-pressure-high-temperature metamorphism during extension in a Jurassic magmatic arc, Central Pontides, Turkey. J Metamorph Geol 32, 49-69.

Okay, A.I., Topuz, G., 2017. Variscan orogeny in the Black Sea region. Int J Earth Sci 106, 569-592.

Okay, A.I., Tüysüz, O., 1999. Tethyan sutures of northern Turkey. The Mediterranean basin: Tertiary extension within the Alpine orogeny. Geol Soc London Spec Pub 156, 475-515.

Okay, A.I., Tüysüz, O., Satır, M., Özkan-Altıner, S., Altıner, D., Sherlock, S., Eren, R.H., 2006. Cretaceous and Triassic subduction-accretion, high-pressure-low-temperature metamorphism, and continental growth in the Central Pontides, Turkey. GSA Bull 118, 1247-1269.

Okay, A.I., Satır, M., Siebel, W., 2006. Pre-Alpide orogenic events in the Eastern Mediterranean region. In: Gee, D.G., Stephenson, R.A. (Eds.), European Lithosphere Dynamics. Geol Soc London 32, 389–405 (Memoirs).

Özgül, N., 2012. Stratigraphy and some structural features of the İstanbul Paleozoic. Turk J Earth Sci 21, 817-866.

Parlak O., 2016. The tauride ophiolites of Anatolia (Turkey): A review. J Earth Sci 27(6), 901-934.

Parlak O., Çolakoğlu A., Dönmez C., Sayak H., Yıldırım N., Türkel A., Odabaşı İ., 2013. Geochemistry and tectonic significance of ophiolites along the Ankara–Erzincan Suture Zone in northeastern Anatolia. In: Robertson, A.H.F., Parlak, O., Ünlügenç, U.C. (Eds.), 2013. Geol Soc London Spec Pub 372, 75-105.

Pattison, D.R.M., 1992. Stability of andalusite and sillimanite and the Al_2SiO_5 triple point: constraints from the Ballachulish Aureole, Scotland. J Geol 100, 423-446.

Pearce, J.A., 1983. Role of the sub-continental lithosphere in magma genesis at active continental margin, in: Hawkesworth, C.J., Norry, M.J. (Eds.), Continental basalts and mantle xenoliths, Shiva, Chenshire, pp. 230-249.

Renne, P.R., Swisher, C.C., Deino, A.L., Karner, D.B., Owens, T.L., DePaolo, D.J. 1998. Intercalibation of standards, absolute ages and uncertainties in $^{40}Ar/^{39}Ar$ dating. Chem Geol 145, 117-152.

Rogers, G., Hawkesworth, C.J., 1989. A geochemical traverse across the north Chilean Andes: Evidence for crust generation from the mantle wedge. Earth Planet Sci Lett 91, 271-285.

Rollinson, H.R., 1993. Using geochemical data: Evaluation, presentation, interpretation. New York, John Wiley & Sons, 352 pp.

Roser, B.P., Korsch, R.J., 1986. Determination of tectonic setting of sandstone-mudstone suites using SiO_2 content and K_2O/Na_2O ratio. J Geol 94, 635-650.

Roser, B.P., Korsch, R.J., 1988. Provenance signatures of sandstone-mudsotone suites determined using discrimination function analysis of major-element data. Chem Geol 67, 119-139.

Şahin S.Y., Güngör Y., Aysal N., Öngen S., 2009. Geochemistry and SHRIMP zircon U–Pb dating of granites within the Strandja and Istanbul Zones (NW Turkey). 62nd Geol Cong Turkey, Ankara, Abstracts, pp 598–599.

Sarıfakıoğlu, E., Özen, H., Winchester, J.A., 2009. Petrogenesis of the Refahiye ophiolite and its tectonic significance for Neotethyan ophiolites along the İzmir-Ankara-Erzincan suture zone. Turk J Earth Sci 18, 187-207.

Sayıt, K., Göncüoglu, M.C., Furman, T., 2010. Petrological reconstruction of Triassic seamounts/oceanic islands within the Palaeotethys: Geochemical implications from the Karakaya subduction/accretion Complex, Northern Turkey. Lithos 119, 501–511.

Şengör, A.M.C., Yılmaz, Y., 1981. Tethyan evolution of Turkey: A plate tectonic approach. Tectonophysics 75, 181-241.

Sosson, M., Rolland, Y., Müller, C., Danelian, T., Melkonyan, R.,, Kekelia, S., Adamia, S., Babazadeh, V., Kangarli, T., Avagyan, A., Galoyan, G., Mosar, J., 2010. Subductions, obduction and collision in the Lesser Caucasus (Armenia, Azerbaijan, Georgia), new insights. Geol Soc London Spec Pub 340, 329-352.

Spear, F.S., Kohn, M.J., Cheney, J.T., 1999. P-T paths from anatectic pelites. Contrib Mineral Petrol 134, 17-32.

Stevens, G., Clemens, J.D., Droop, G.T.R., 1997. Melt production during granulite-facies anatexis: experimental data from "primitive" metasedimentary protoliths. Contrib Mineral Petrol 128, 352-370.

Sunal, G. 2013. Devonian magmatism in the western Sakarya Zone, Karacabey region, NW Turkey. Geodin Acta 25(3-4), 183-201.

Taylor, S.R., McLennan, S.M., 1981. The composition and evolution of the continental crust, rare element evidence from sedimentary rocks. Philos Trans R Soc A 301, 381-399.

Taylor, S.R., McLennan, S.M., 1985. The continental crust: Its composition and evolution. Blackwell Scientific Publication, Carlton, 312 pp.

Tekin, U.K., Göncüoğlu, M.C., Pandolfi, L., Marroni, M., 2012. Middle Late Triassic radiolarian cherts from the Arkotdağ melange in northern Turkey: implications for the life span of the northern Neotethyan branch. Geodin Acta 25, 305-319.

Topuz, G., Altherr, R., Kalt, A., Satır, M., Werner, O., Schwarz, W.H., 2004. Aluminous granulites from the Pulur complex, NE Turkey: a case of partial melting, efficient melt extraction and crystallization. Lithos 72, 183–207.

Topuz, G., Çelik, Ö.F., Şengör, A.M.C., Altıntaş, İ.E., Zack, T., Rolland, Y., Barth, M., 2013b. Jurassic ophiolite formation and emplacement as backstop to a subduction-

accretion complex in Northeast Turkey, the Refahiye Ophiolite, and relation to the Balkan Ophiolites. Am J Sci 313, 1054-1087.

Topuz, G., Göçmengil, G., Rolland, Y., Çelik, Ö.F., Zack, T., Schmitt, A.K., 2013a. Jurassic accretionary complex and ophiolite from northeast Turkey: No evidence for the Cimmerian continental ribbon. Geology 41, 255-258.

Uğuz, M., Sevin, F., 2007. Geological map series of Turkey, Kastamonu-E32 quadrangle: Turkey MTA (Mineral Research & Exploration General Directorate), scale 1:100 000, 1 sheet.

Ustaömer, P.A., Mundil, R., Renne, P.R., 2005. U/Pb and Pb/ Pb zircon ages for arc-related intrusions of the Bolu Massif (W Pontides, NW Turkey): Evidence for Late Precambrian (Cadomian) age. Terra Nova 17, 215-223.

Ustaömer, P.A., Ustaömer, T., Robertson, A.H.F., 2012. Ion Probe U-Pb Dating of the Central Sakarya Basement: A peri-Gondwana Terrane Intruded by Late Lower Carboniferous Subduction/Collision-related Granitic Rocks. Turk J Earth Sci 21, 905-932.

Ustaömer, T., Robertson, A.H.F., 1999. Geochemical evidence used to test alternative plate tectonic models for pre-Upper Jurassic (Palaeotethyan) units in the Central Pontides, N Turkey. Geol J 34, 25-53.

Ustaömer, T., Ustaömer, P.A., Robertson, A.H.F., Gerdes, A., 2016. Implications of U–Pb and Lu–Hf isotopic analysis of detrital zircons for the depositional age, provenance and tectonic setting of the Permian-Triassic Palaeotethyan Karakaya Complex, NW Turkey. Int J Earth Sci 105, 7–38.

Whitney, D.L., Evans, B.W., 2010. Abbreviations for names of rock-forming minerals. Am Mineral 95, 185-187.

Winchester, J.A., 1984. Element mobility associated with synmetamorphic shear zones Near Scotchport, NW Mayo, Ireland. J Metamorph Geol 2, 1-11.

Winchester, J.A., Max, M.D., 1982. The geochemistry and origin of the Precambrian rocks of the Rosslare Complex, SE Ireland. J Geol Soc London 139, 309-319.

Yardley, B.W.D., 1990. An Introduction to Metamorphic Petrology, Longman Scientific and Technical, Longman, 248 pp.

Yılmaz, A., Yılmaz., H., 2013. Ophiolites and Ophiolitic Mélanges of Turkey: A Review. Geol Bull Turkey 56, 61-114.

Yılmaz, O., 1980. Lithostratigraphic units and tectonics of northeastern part of the Daday-Devrekani Massive (Western Pontides, Turkey). Yerbilimleri 5-6, 101-135.

Figure captions

Fig. 1. (a) Map of the main tectonic units of Turkey (modified after Okay and Tüysüz, 1999) and the tectonic relationships between metamorphic massifs and basement (modified from Atalay, 1987; Okay, 2008). **(b)** Geological map of the northern part of Central Pontides (Okay et al., 2014). **(c)** Generalized geological map of the Devrekani Massif and surrounding areas (modified after Altun et al., 1990; Uğuz and Sevin, 2007). IZT: Istanbul-Zonguldak Terrane, SCT: Sakarya Composite Terrane, ATT: Anatolide-Tauride Terrane, IPSB: Intra-Pontide Suture Belt, IAESB: Izmir-Ankara-Erzincan Suture Belt.

Fig. 2. Detailed geological map showing the distribution of metacarbonates, paragneisses, orthogneisses and amphibolites in the Devrekani Massif.

Fig. 3. Field photographs of paragneisses and related rocks from the massif. **(a)** Gneisses form the lower parts and metacarbonate form the upper parts. **(b-c)** Gneisses and amphibolite assemblages in the massif. **(d)** A hand specimen of a paragneiss with irregular folds rich in biotite (dark). **(e-f)** Well-developed centimeter-spaced gneissic banding with symmetric, asymmetric and irregular folds.

Fig. 4. Photomicrographs from the Devrekani paragneisses (a and b images were taken in plane polarized, others in cross-polarized light). **(a)** Garnet is present as subhedral- to anhedral-crystals up to 1 mm in size and contains quartz, biotite, feldspar and ilmenite inclusions. Biotite flakes associated with garnet porphyroblasts in biotite-rich bands. **(b)** Gneisses with garnet, sillimanite, pinitized cordierite, biotite and hercynite. **(c-d)** Strongly foliated rocks dominated by sillimanite, biotite and cordierite with quartz, feldspar and opaque minerals. **(e)** Pinitized cordierite porphyroblasts with biotite (brown) and quartz. **(f-g)** Gneisses with cordierite, biotite, sillimanite, garnet and quartz. **(h)** Coarse anhedral cordierite crystals partially or completely envelope euhedral garnet grains.

Fig. 5. Alm + Sps, Grs and Pyp ternary diagram showing the compositions of garnet in GB and GSCB gneisses from the Devrekani paragneisses, and thin section microphotographs of garnet minerals showing different morphologies.

Fig. 6. Chemical classification and variation diagrams of the feldspar and spinel-group minerals from the Devrekani paragneisses. **(a)** Or-Ab-An triangular plot of feldspar minerals, **(b)** Cr/(Cr+Al) vs. $Mg/(Mg+Fe^{2+})$ classification diagram of spinel-group minerals and microphotographs of cordierite with inclusions of biotite, sillimanite, hercynite (dark green) and garnet.

Fig. 7. (a) $^{38}Ar_{Cl}/^{39}Ar_{K}$ vs. age plot for GSCB gneiss sample H3. **(b)** Weighted mean of ^{40}Ar-^{39}Ar age diagram for GB gneiss sample KD1 and **(c)** SCB gneiss sample KD7B.

Fig. 8. Normalized trace element diagrams for the protoliths of the Devrekani paragneisses. **(a)** MORB (Pearce, 1983) and **(b)** PAAS normalized trace element diagrams. **(c)** Chondrite (Boynton, 1984) and **(d)** PAAS normalized REE diagrams. UC: upper continental crust (compositions from Taylor and McLennan, 1981), NASC: North American shale composite from Gromet et al. (1984), PAAS: Post-Archaean average Australian sedimentary rock (compositions from McLennan, 1989).

Fig. 9. Pressure-temperature diagram of the Devrekani Massif. Peak metamorphism is constrained by the intersection of equilibria derived from the GASP barometer with Na-in cordierite and garnet-biotite equilibria. High-temperature decompression was determined from the Crd + Hc assemblage. Al_2SiO_5 triple point and Sil/Ky transition of Pattison (1992). Alm + Sil = Hc + Crd, H_2O-saturated metapelite solidus and Ms+Qtz dehydration-melting according to Spear et al. (1999). Bt + Sil + Qtz + Pl = Grt + Crd + Kfs + Melt from Le Breton and Thompson (1988); Stevens et al. (1997). Thermometers: Na-in cordierite (Mirwald, 1986); Grt–Bt Fe-Mg exchange (Ferry and Spear, 1978). Barometers: GASP; garnet-sillimanite-quartz-plagioclase, GRIPS; garnet-rutile-ilmenite-plagioclase-quartz, GRAIL; garnet-rutile-sillimanite-ilmenite-quartz (references for calibration of barometers see Table 4).

Fig. 10. Geochemical discrimination diagrams for the protoliths. **(a)** Zr/TiO_2 vs. Ni plot distinguishing igneous from sedimentary fields (Winchester and Max, 1982), **(b)** Log ($Fe_2O_3^T/K_2O$) vs. (SiO_2/Al_2O_3) classification diagram (Herron, 1988), **(c)** Discriminant function diagram for the provenance signatures of sandstone-mudstone suites (Roser and Korsch, 1988), **(d)** Th vs. Sc diagram from McLennan et al. (1993), **(e)** La vs. Th diagram from Taylor and McLennan (1985), **(f)** K_2O/Na_2O vs. SiO_2 discrimination diagram of Roser and Korsch (1986) for sandstone-mudstone suites.

Fig. 11. ^{40}Ar-^{39}Ar biotite cooling ages with data from other rocks from the Devrekani Massif. Each vertical solid line represents a single biotite (bt) or hornblende (hbl) age. Amphibolite ages are from Gücer (2014) and orthogneiss data from Gücer et al. (2016).

Fig. 12. Simplified tectonic model (modified from Gücer et al., 2016) showing the Middle – Upper Jurassic geodynamic evolution of the Devrekani Massif in Central Pontides (N Turkey).

Table captions

Table 1. Mineral assemblages of the Devrekani paragneisses.

Table 2. Summary of ^{40}Ar-^{39}Ar and U-Pb Zircon ages from the Devrekani Massif.

Table 3. Summary of temperature estimates from the Devrekani paragneisses.

Table 4. Pressure estimates for GB and GSCB gneisses from the Devrekani paragneisses.

Supplementary Table captions

Table S1. Representative electron microprobe analyzes of garnet, biotite, plagioclase, K-feldspar, cordierite, sillimanite, hercynite and Fe-Ti oxide minerals for the Devrekani paragneisses.

Table S2. ^{40}Ar-^{39}Ar biotite dating data for the Devrekani paragneisses.

Table S3. Representative major oxide (wt%), trace (ppm) and rare earth (ppm) element concentrations of the Devrekani paragneisses.

Table S4. Thermometer and barometer results from the Devrekani paragneisses.

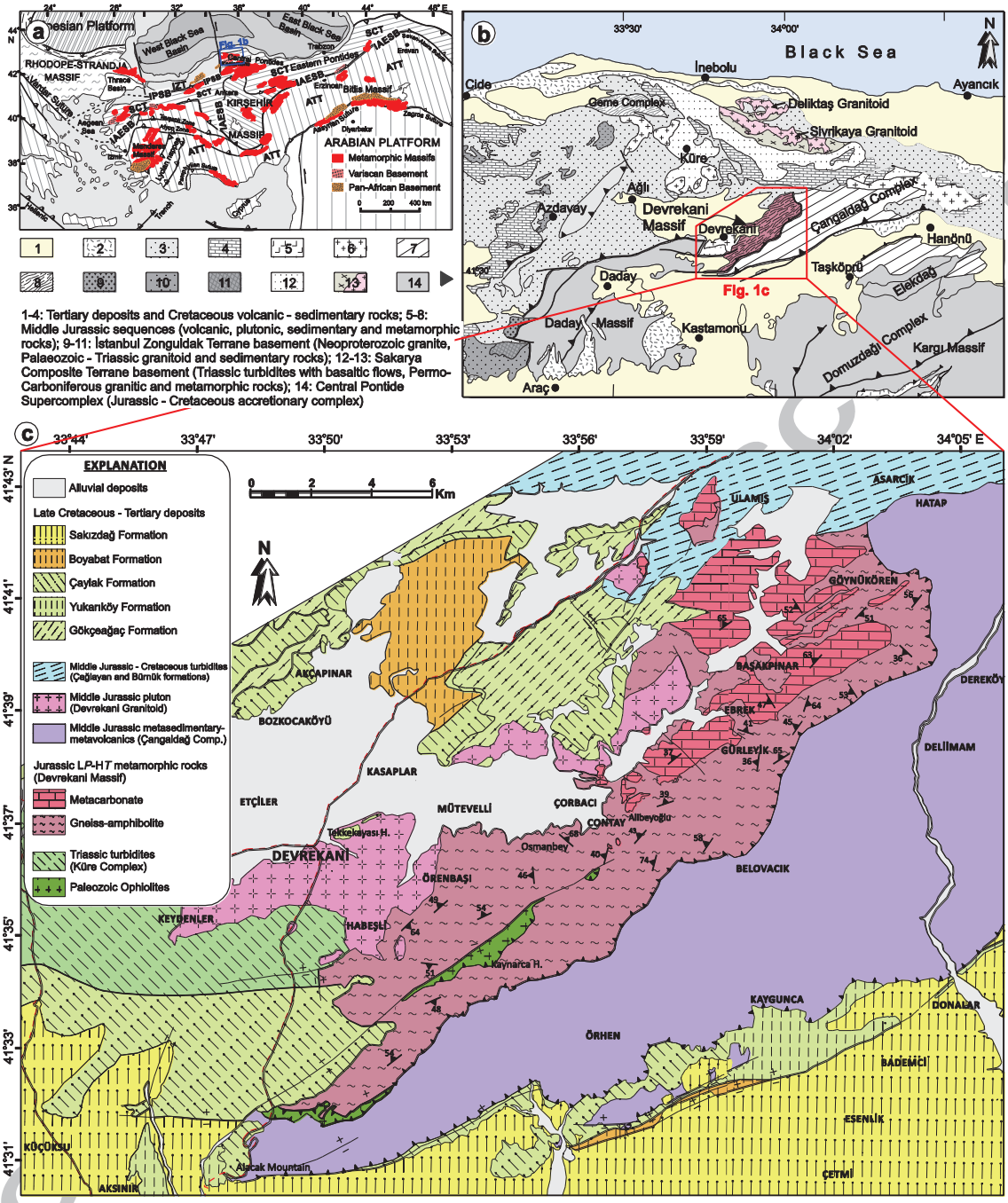

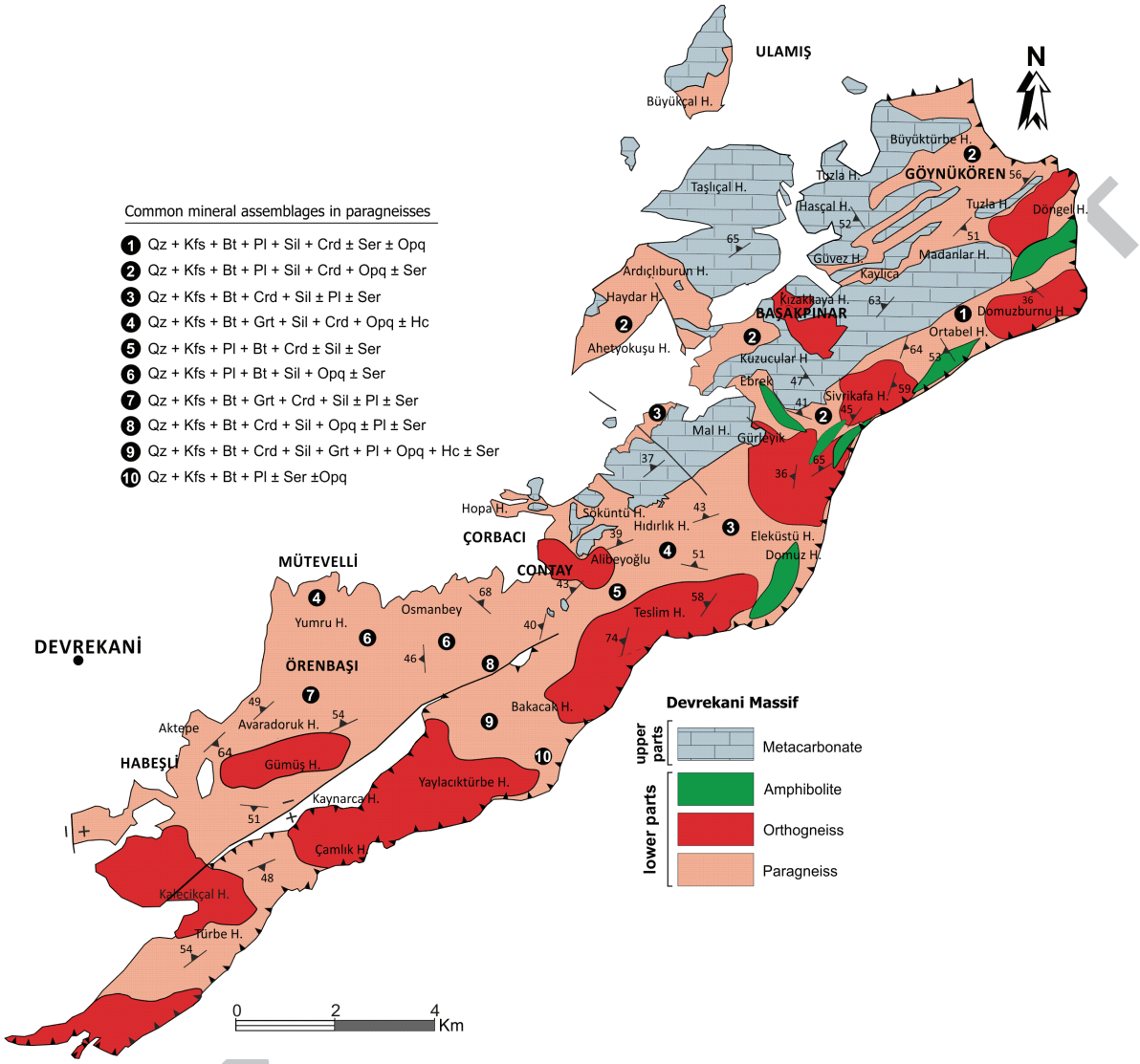

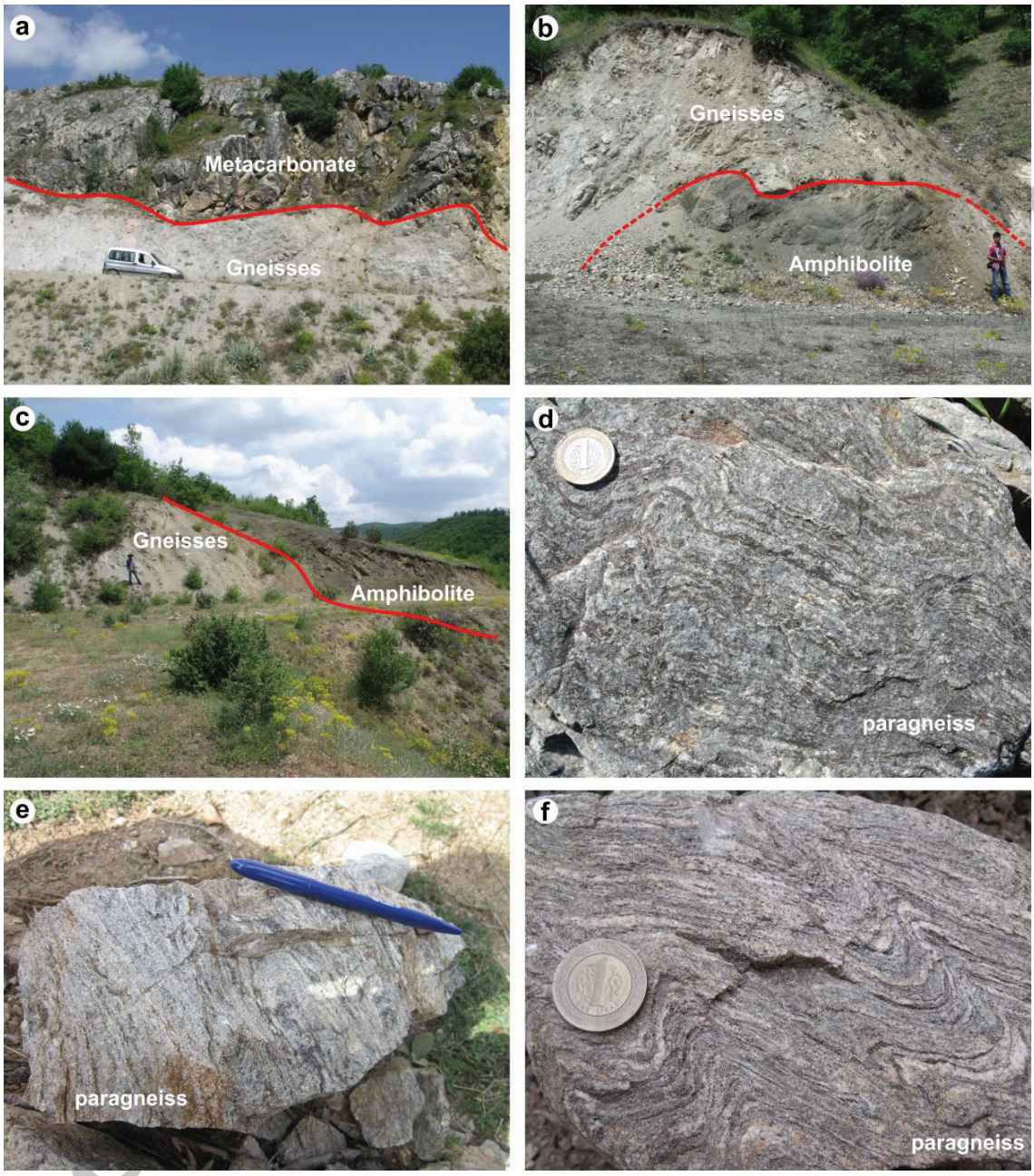

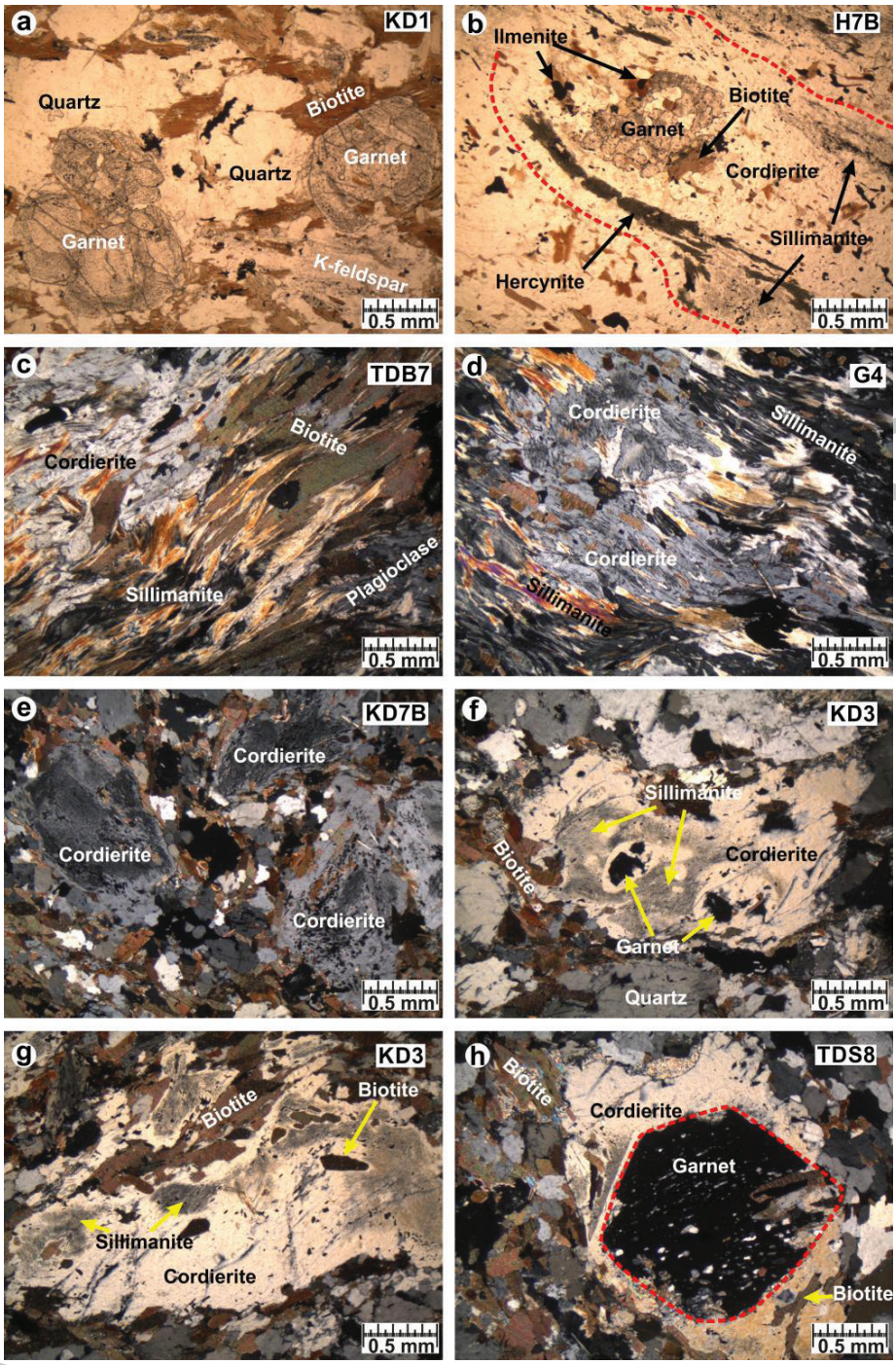

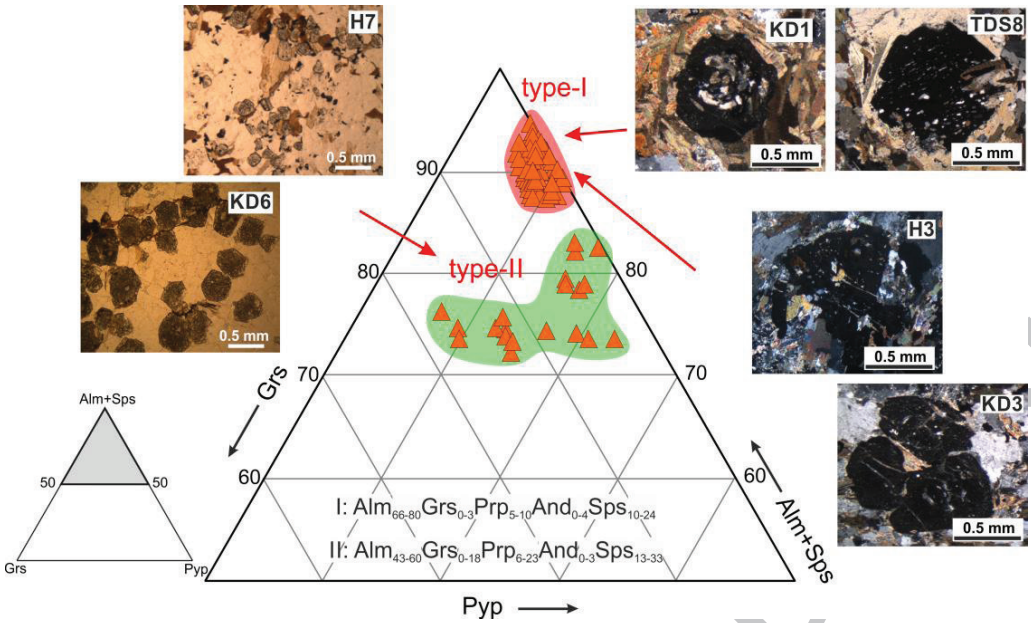

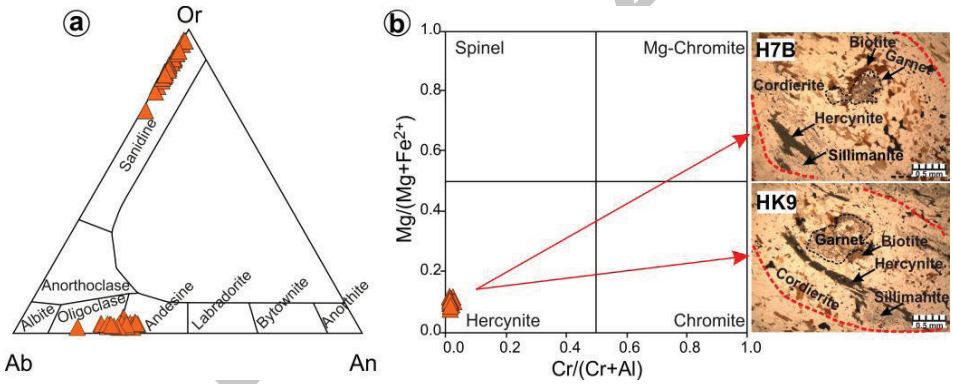

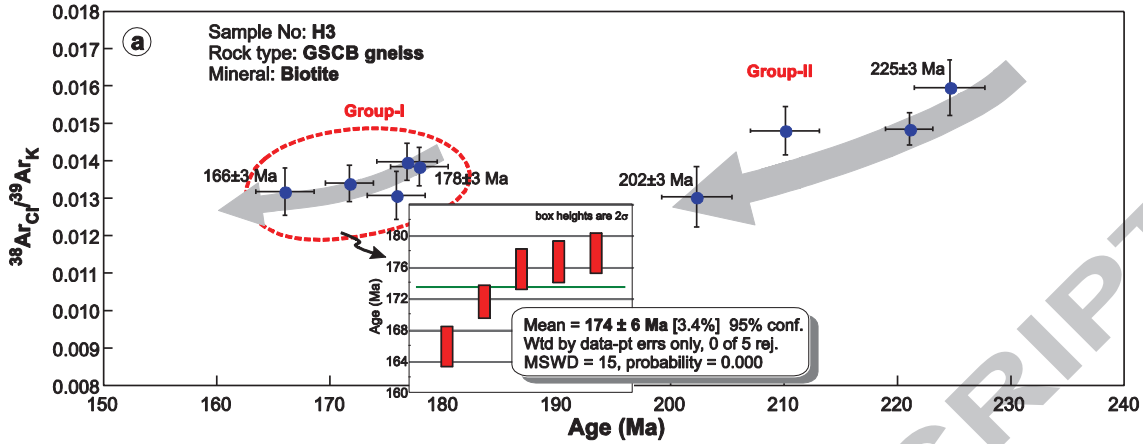

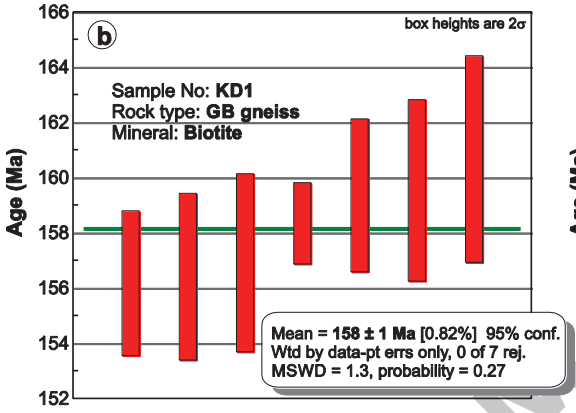

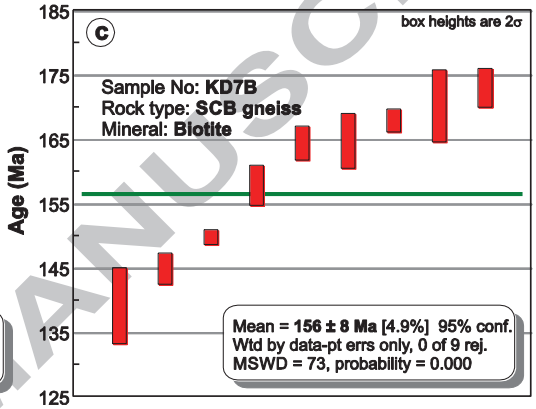

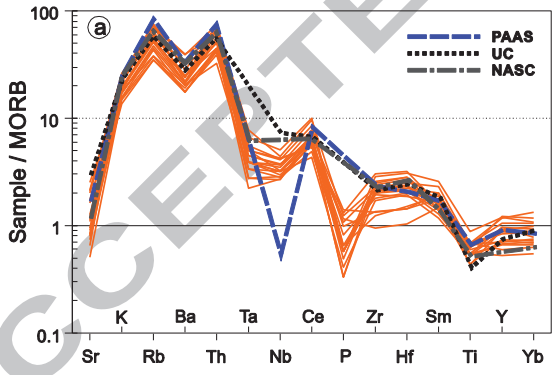

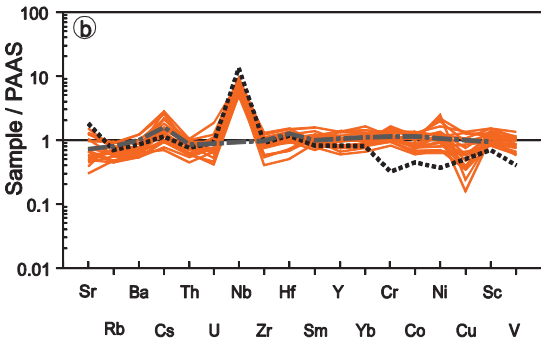

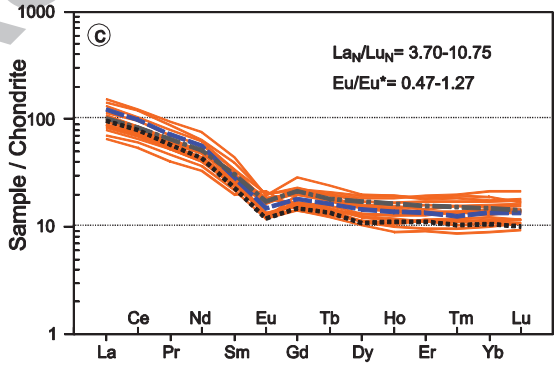

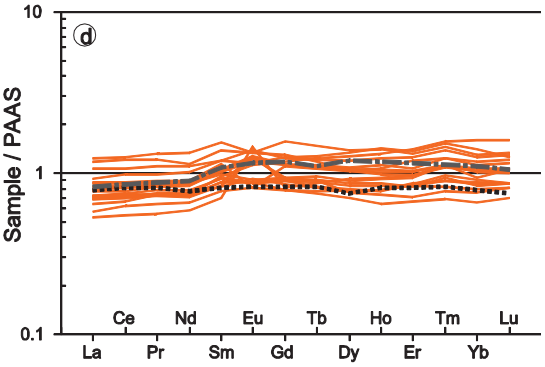

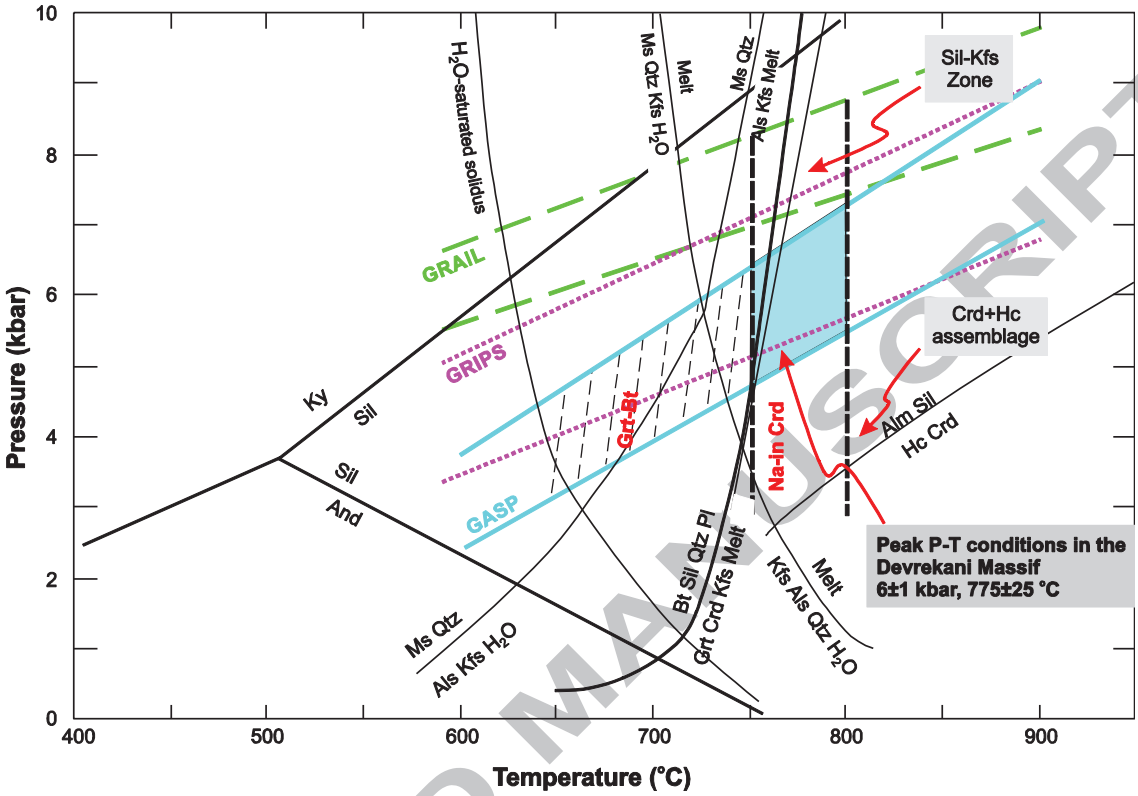

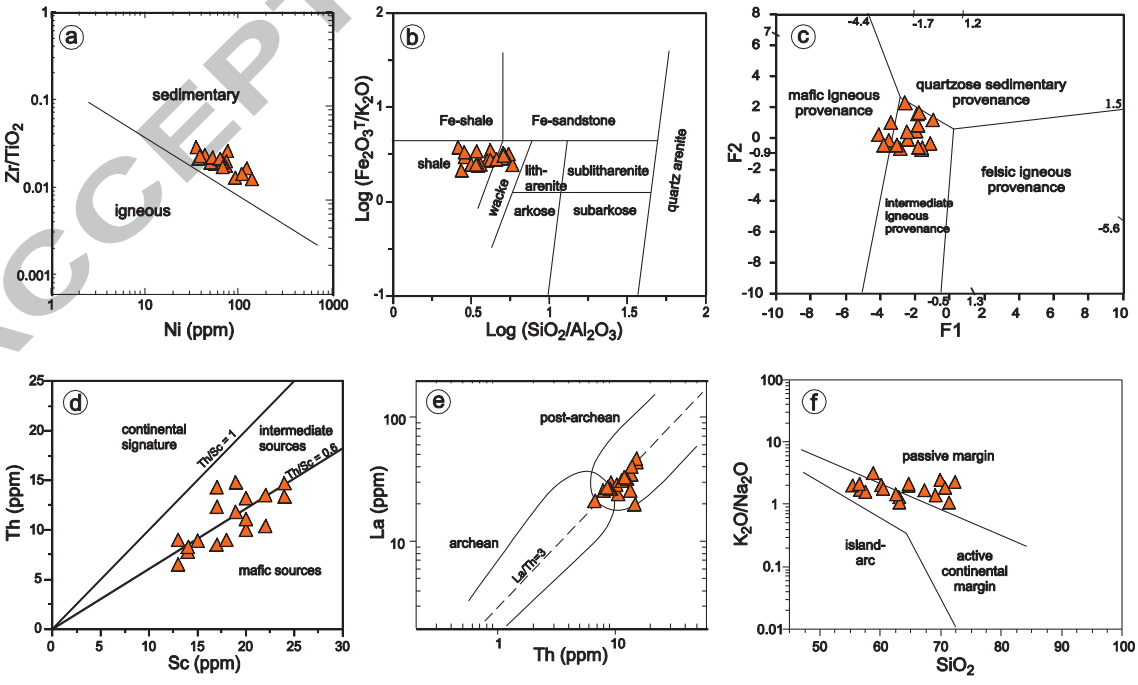

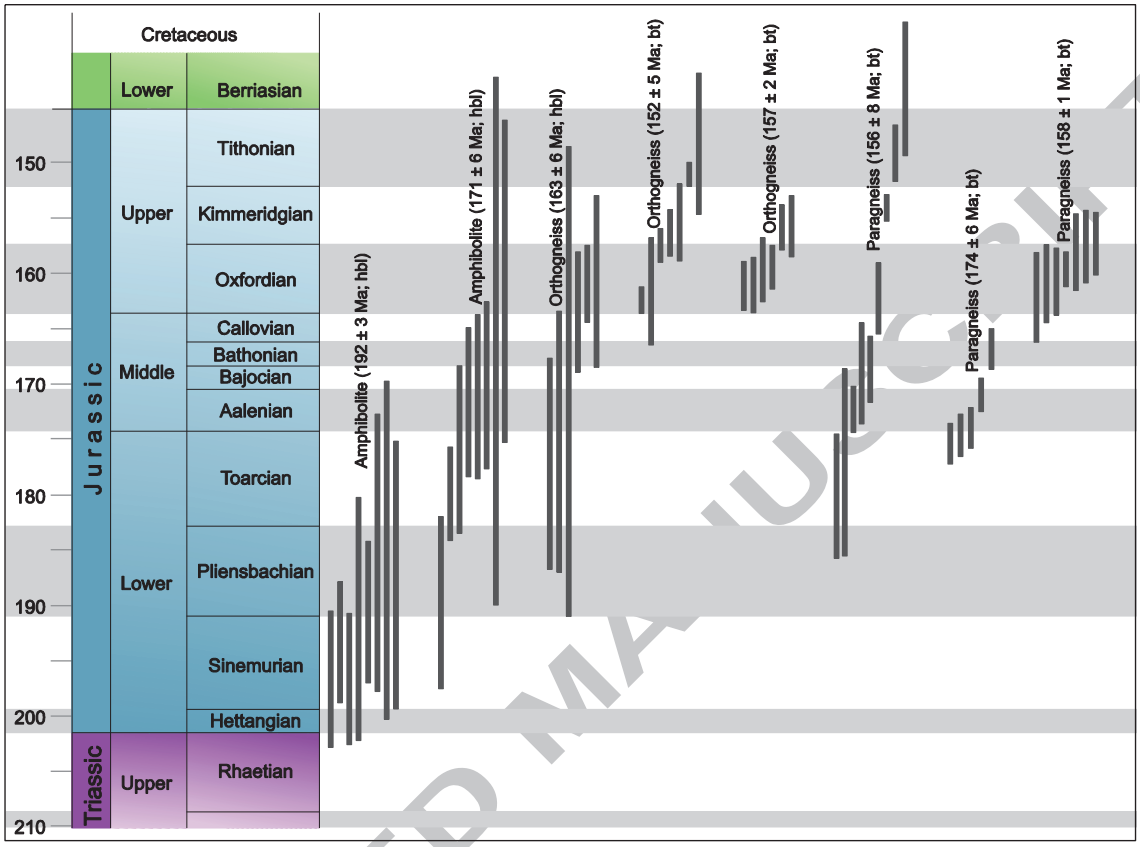

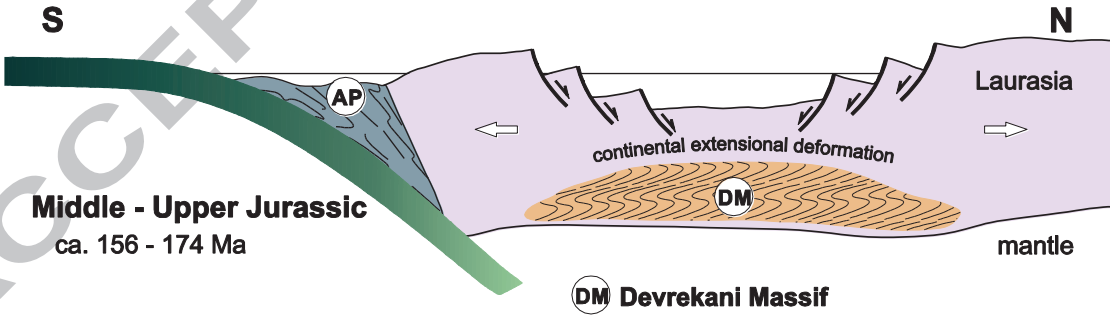

Middle - Upper Jurassic
ca. 156 - 174 Ma

AP Accretionary prisms

- Triassic
- Jurassic

DM Devrekani Massif

Variscan metamorphic basement of Sakarya zone

Upper amphibolite - lower granulite high temperature metamorphism (6±1 kbar; 775±25°C)

- paragneiss
- orthogneiss
- amphibolite
- metacarbonate
- quartzite

Table 1. Mineral assemblages of the Devrekani paragneisses

Samples	Ms	Qz	Pl	Kfs	Bt	Sil	Grt	Crd	Hc	Qpq	Chl	Ser	Spn	Zr	Ap
Sillimanite-biotite (SB) gneisses (mainly shows fibrolepidogranoblastic texture)															
DB3A	+	++	++	++	++	++	--	⊕	--	+	*	**	--	⊕	--
Garnet-biotite (GB) gneisses (mainly shows porphyroblastic texture)															
KD1	--	++	++	++	++	+	++	--	--	+	--	**	--	⊕	⊕
Cordierite-biotite (CB) gneisses (mainly shows lepidogranoblastic texture)															
D712	+	++	+	++	++	+	--	++	+	+	--	**	--	⊕	--
DB3	+	++	+	++	++	+	--	++	--	+	--	**	--	--	--
HK8	+	++	+	++	++	+	--	++	+	+	--	**	⊕	⊕	--
HK9	⊕	++	+	++	++	+	--	++	+	+	--	**	--	⊕	--
KD7	--	++	+	++	++	⊕	--	++	--	+	--	--	⊕	⊕	--
KM2	--	++	+	++	++	+	--	+	--	+	--	--	--	⊕	--
TDS11	⊕	++	+	+	++	+	⊕	++	--	+	--	**	⊕	⊕	--
TDS16A	⊕	++	+	++	++	⊕	--	++	--	+	--	**	--	--	--
Sillimanite-cordierite-biotite (SCB) gneisses (mainly shows fibrolepidogranoblastic texture)															
DB6	--	++	++	+	++	++	--	++	--	+	*	**	--	--	--
KD7B	⊕	++	--	--	++	++	--	++	--	+	--	--	--	⊕	--
KD8	⊕	++	--	--	++	+	--	++	--	+	--	--	⊕	⊕	--
KD9	⊕	++	+	+	++	++	--	++	--	+	--	**	--	⊕	--
TDS12	+	++	+	++	++	++	--	++	--	+	--	**	--	--	⊕
TDS13	--	++	+	+	++	++	--	++	--	+	--	**	--	--	--
TDS5	+	++	+	+	++	++	--	++	+	+	--	**	--	⊕	--
TDS7	+	++	⊕	+	++	++	--	++	--	+	--	**	--	⊕	--
DA5B	--	++	++	++	++	++	--	++	--	+	--	**	--	--	--
DG5	⊕	++	++	+	++	++	--	++	--	+	--	**	--	⊕	--
G4	⊕	++	++	++	++	++	--	++	--	+	*	**	--	--	--
TDB7	⊕	++	++	+	++	++	--	++	⊕	+	--	**	--	--	--
Garnet-sillimanite-cordierite-biotite (GSCB) gneisses (mainly shows fibrolepidogranoblastic texture)															

D711	⊕	++	++	++	++	+	++	++	--	+	--	**	⊕	⊕	--
D713	⊕	++	++	++	++	+	+	++	+	+	--	**	--	⊕	--
D718	⊕	++	++	++	++	+	++	++	--	+	--	**	--	⊕	--
H7	+	++	++	++	++	+	++	++	--	+	--	**	⊕	⊕	--
KD6	--	++	++	++	++	--	++	++	--	+	--	--	--	⊕	--
TDO10	⊕	++	++	++	++	+	++	++	--	+	--	**	⊕	⊕	--
TDO12B	⊕	++	++	++	++	+	++	++	+	+	*	**	⊕	--	--

++ major constituent (>5%); + minor constituent (1-5%); ⊕ accessory phase (≤1%); * secondary minerals. (from minerals and/or veins); ** secondary minerals (from feldspar and cordierite); -- not observed. Ms: Muscovite, Qz: Quartz, Pl: Plagioclase, Kfs: K-feldspar, Bt: Biotite, Sil: Sillimanite, Grt: Garnet, Crd: Cordierite, Hc: Hercynite, Opq: Opaques, Chl: Chlorite, Ser: Sericite, Spn: Sphene, Zrn: Zircon and Ap: Apatite (mineral abbreviations after Whitney and Evans, 2010).

Table 1. Continued

Samples	Ms	Qz	Pl	Kfs	Bt	Sil	Grt	Crd	Hc	Qpq	Chl	Ser	Spn	Zr	Ap
D706	⊕	++	⊕	+	++	++	+	++	--	+	--	**	⊕	⊕	--
H3	⊕	++	+	++	++	+	+	++	+	+	--	**	--	⊕	--
H3B	⊕	++	+	++	++	+	+	++	+	+	--	**	--	⊕	--
H7B	--	++	++	++	++	++	++	++	+	+	--	**	⊕	⊕	--
KD2	--	++	++	++	++	++	++	++	--	+	--	**	--	⊕	--
KD3	--	++	+	++	++	++	+	++	--	+	--	**	--	⊕	--
TDG3	--	++	++	+	++	++	+	++	--	+	--	**	⊕	⊕	--
TDG4	--	++	++	+	++	++	++	++	--	+	--	**	--	⊕	--
TDS8	--	++	+	+	++	++	++	++	--	+	--	**	--	--	--
TDS9	--	++	++	++	++	+	+	+	+	+	--	**	--	⊕	--
TDS10	--	++	+	+	++	++	+	++	--	+	--	**	⊕	⊕	--
TDS19	--	++	++	+	++	+	+	++	+	+	--	**	--	--	--

++ major constituent (>5%); + minor constituent (1-5%); ⊕ accessory phase (≤1%); * secondary minerals. (from minerals and/or veins); ** secondary minerals (from feldspar and cordierite); -- not observed. Ms: Muscovite, Qz: Quartz, Pl: Plagioclase, Kfs: K-feldspar, Bt: Biotite, Sil: Sillimanite, Grt: Garnet, Crd: Cordierite, Hc: Hercynite, Opq: Opaques, Chl: Chlorite, Ser: Sericite, Spn: Sphene, Zrn: Zircon and Ap: Apatite (mineral abbreviations after Whitney and Evans, 2010).

Table 2. Summary of ^{40}Ar-^{39}Ar and U-Pb Zircon ages from the Devrekani Massif

Sample No	Ar-Ar ages (Ma)		U-Pb zircon ages (Ma)	
	Age range	Mean age	Age range	Mean age
Paragneisses (this study)				
KD7B	139 – 173 (n= 9)	156 ± 8 (biotite)		
KD1	152 – 164 (n= 10)	158 ± 1 (biotite)		
H3	166 – 225 (n= 9)	174 ± 6 (biotite)		
Orthogneisses (from Gücer et al., 2016)				
DG9	144 – 159 (n= 7)	152 ± 5 (biotite)	209 – 276 (n=16)	268 ± 5
G3	149 – 160 (n= 10)	157 ± 2 (biotite)	158 – 320 (n=23)	316 ± 9
DB14	155 – 159 (n= 2, biotite)			
DB14	160 – 176 (n= 6)	163 ± 6 (hornblende)		
DA3			176 – 302 (n=28)	253 ± 9
Amphibolite (from Gücer, 2014)				
DB8	176 – 196 (n= 9)	192 ± 3 (hornblende)		
TDB10	154 – 184 (n= 8)	171 ± 6 (hornblende)		

Table 3. Summary of temperature estimates from the Devrekani paragneisses

Na-in-cordierite thermometer			
Sample	**Na content (cpfu)**	**$T_{MIN} - T_{MAX}$ (°C)**	**Calibration**
H3 (GSCB gneiss)	0.040 (n= 10)	747 - 794	Mirwald (1986)
HK9 (CB gneiss)	0.036 (n= 12)	744 - 800	
KD7B (SCB gneiss)	0.038 (n= 12)	747 - 808	
KD3 (GSCB gneiss)	0.033 (n=3)	770 - 800	
H7B (GSCB gneiss)	0.038 (n= 5)	763 - 794	
H7 (GSCB gneiss)	0.055 (n= 5)	698 - 741	
DB3 (CB gneiss)	0.035 (n= 3)	764 - 798	
G4 (SCB gneiss)	0.044 (n= 2)	734 - 776	
Garnet-biotite thermometer			
Sample	**Analysis No**	**T (°C) at assumed P of 6 kbar**	
H3 (GSCB Gneiss)	C1-33/C1-6	622 ± 15	Ferry and Spear (1978)
H3 (GSCB Gneiss)	C1-38/C1-6	680 ± 17	
H7 (GSCB Gneiss)	C2-9/C2-17	668 ± 33	
H7 (GSCB Gneiss)	C4-2/C2-3	801 ± 49	
H7B (GSCB Gneiss)	C1-8/C1-20	633 ± 15	
H7B (GSCB Gneiss)	C1-10/C1-17	822 ± 20	
KD1 (GB Gneiss)	C3-23/C3-34	734 ± 25	
KD1 (GB Gneiss)	C3-21/C3-33	821 ± 32	
KD3 (GSCB Gneiss)	C3-17/C3-44	619 ± 32	
KD3 (GSCB Gneiss)	C3-13/C3-31	753 ± 52	
KD6 (GSCB Gneiss)	C2-19/C2-6	698 ± 34	
KD6 (GSCB Gneiss)	C2-25/C2-40	749 ± 35	
Garnet-cordierite thermometer			
Sample	**Analysis No**	**T (°C) at assumed P of 6 kbar**	
H7 (GSCB Gneiss)	see supplementary Table A4	653±5 (n= 10)	Bhattacharya et al., (1988)
H7 (GSCB Gneiss)		709±22 (n= 18)	
H7B (GSCB Gneiss)		689±12 (n= 10)	
KD3 (GSCB Gneiss)		671±8 (n= 12)	
H3 (GSCB Gneiss)		662±5 (n= 7)	

Table 4. Pressure estimates for GB and GSCB gneisses from the Devrekani paragneisses

Sample	Barometer	*P* (kbar) at assumed *T* of		
		750 °C	800 °C	Calibration of barometers
H7/1	GASP	5.4 ± 0.4	6.2 ± 0.4	
H7B/1	GASP	5.8 ± 0.7	6.7 ± 0.7	
KD3/1	GASP	5.7 ± 0.6	6.6 ± 0.7	
KD6	GASP	5.7 ± 0.2	6.5 ± 0.2	Koziol (1989)
H7/2	GASP	6.3 ± 0.8	7.1 ± 0.8	
H7B/2	GASP	6.4 ± 0.7	7.3 ± 0.7	
KD3/2	GASP	6.2 ± 0.2	7.0 ± 0.2	
H7	GRIPS	5.7 ± 0.4	6.2 ± 0.4	
H7B	GRIPS	6.6 ± 0.4	7.2 ± 0.4	Bohlen and Liotta (1986)
KD6	GRIPS	6.3 ± 0.6	6.9 ± 0.6	
H7	GRAIL	7.6 ± 0.2	8.0 ± 0.2	
H7B	GRAIL	8.1 ± 0.1	8.6 ± 0.1	Bohlen et al. (1983)
KD6	GRAIL	7.5 ± 0.2	8.0 ± 0.2	

GA

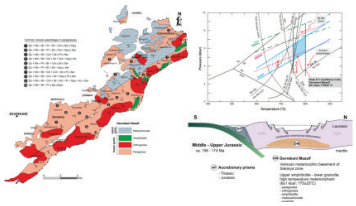

Highlights

- The protoliths of paragneisses are composed of pelitic sediments including shale and wackestone.
- The protoliths are linked to a pre-Jurassic sedimentation and a continental arc magmatism.
- The Devrekani Massif was exposed to a Jurassic MP/HT metamorphism (ca. 156 Ma).
- The Jurassic HT metamorphism developed in an extensional tectonic environment.

CONFLICT OF INTEREST

The authors have not declared any conflict of interests.